

Characterization of Aerosol Composition, Aerosol Acidity and Organic Acid Partitioning at an Agriculture-Intensive Rural Southeastern U.S. Site

Theodora Nah,^{1,a} Hongyu Guo,¹ Amy P. Sullivan,² Yunle Chen,¹ David J. Tanner,¹ Athanasios Nenes,^{1,3,4,5} Armistead Russell,⁶ Nga Lee Ng,^{1,3} L. Gregory Huey¹ and Rodney J. Weber^{1,*}

¹*School of Earth and Atmospheric Sciences, Georgia Institute of Technology, Atlanta, GA, USA*

²*Department of Atmospheric Science, Colorado State University, Fort Collins, CO, USA*

³*School of Chemical and Biomolecular Engineering, Georgia Institute of Technology, Atlanta, GA, USA*

⁴*ICE-HT, Foundation for Research and Technology, Hellas, 26504 Patras, Greece*

⁵*IERSD, National Observatory of Athens, P. Penteli, 15236, Athens, Greece*

⁶*School of Civil and Environmental Engineering, Georgia Institute of Technology, Atlanta, GA, USA*

^a*Now at School of Energy and Environment, City University of Hong Kong, Kowloon, Hong Kong, China*

* To whom correspondence should be addressed: rweber@eas.gatech.edu

Abstract

The implementation of stringent emission regulations has resulted in the decline of anthropogenic pollutants including sulfur dioxide (SO₂), nitrogen oxides (NO_x) and carbon monoxide (CO). In contrast, ammonia (NH₃) emissions are largely unregulated, with emissions projected to increase in the future. We present real-time aerosol and gas measurements from a field study conducted in an agricultural-intensive region in the southeastern U.S. during the fall of 2016 to investigate how NH₃ affects particle acidity and secondary organic aerosol (SOA) formation via the gas-particle partitioning of semi-volatile organic acids. Particle water and pH were determined using the ISORROPIA-II thermodynamic model and validated by comparing predicted inorganic HNO₃-NO₃⁻ and NH₃-NH₄⁺ gas-particle partitioning ratios with measured values. Our results showed that despite the high NH₃ concentrations (average 8.1 ± 5.2 ppb), PM₁ were highly acidic with pH values ranging from 0.9 to 3.8, and an average pH of 2.2 ± 0.6 . PM₁ pH varied by approximately 1.4 units diurnally. Formic and acetic acids were the most abundant gas-phase organic acids, and oxalate was the most abundant particle-phase water-soluble organic acid anion. Measured particle-phase water-soluble organic acids were on average 6 % of the total non-refractory PM₁ organic aerosol mass. The measured molar fraction of oxalic acid in the particle phase (i.e., particle-phase oxalic acid molar concentration divided by the total oxalic acid molar concentration) ranged between 47 and 90 % for PM₁ pH 1.2 to 3.4. The measured oxalic acid gas-particle partitioning ratios were in good agreement with their corresponding thermodynamic predictions, calculated based on oxalic acid's physicochemical properties, ambient temperature, particle water and pH. In contrast, gas-particle partitioning of formic and acetic acids were not well predicted for reasons

currently unknown. For this study, higher NH_3 concentrations relative to what has been measured in the region in previous studies had minor effects on PM_{10} organic acids and their influence on the overall organic aerosol and PM_{10} mass concentrations.

1. Introduction

Ammonia (NH_3) is the most abundant basic gas in the troposphere and plays an important role in many atmospheric processes. It is a major neutralizer of atmospheric acidic species, reacting readily with sulfuric acid (H_2SO_4) and nitric acid (HNO_3) to form ammonium sulfate and nitrate salts (e.g., $(\text{NH}_4)_2\text{SO}_4$, and other forms such as NH_4HSO_4 , $(\text{NH}_4)_3\text{H}(\text{SO}_4)_2$, and NH_4NO_3), which are often the main inorganic components of atmospheric aerosols. The formation of particle-phase ammonium sulfate and nitrate salts in the aerosol phase depends on the thermodynamic states of their precursors and the environmental conditions, which can consequently affect aerosol pH. For example, Guo et al. (2017b) showed that for Southeast U.S. summertime conditions, as aerosol pH increases, the relative fractions of SO_4^{2-} and HSO_4^- increases and decreases, respectively. Wet and dry deposition are the principle NH_3 sinks (Dentener and Crutzen, 1994). NH_3 is spatially heterogeneous, with the highest concentrations typically found near emission sources (Seinfeld and Pandis, 2016). The dominant NH_3 sources in rural areas are agricultural in nature, and include the application of fertilizers and volatilization of livestock waste (Reis et al., 2009; Ellis et al., 2013; Van Damme et al., 2014). Biomass burning, either from wildfires or from controlled burning during land-clearing operations, is also a significant source of NH_3 in rural environments. The primary source of NH_3 in urban areas are industrial emissions (e.g., NH_3 synthesis, manufacture of ammonium nitrate and urea, fluid and thermal catalytic cracking processes in petroleum refinery), though vehicular emissions can be a significant NH_3 source in some heavily populated cities (Reis et al., 2009; Lamarque et al., 2010; Yao et al., 2013; Sun et al., 2017). Vehicular NH_3 emissions are thought to be produced primarily from the reaction of nitrogen oxide with hydrogen in the presence of carbon monoxide in three-way catalysts of gasoline light duty vehicles (Barbier-Jr and Duprez, 1994; Whittington et al., 1995; Livingston et al., 2009; Suarez-Bertoa et al., 2014).

In the US, implementation of stringent emission controls on traditional anthropogenic air pollutants, such as sulfur dioxide (SO_2), nitrogen oxides (NO_x) and carbon monoxide (CO), have led to steady decreases in their emissions, and consequently their concentrations (Blanchard et al., 2013b; Xing et al., 2013). In contrast, NH_3 emissions are largely unregulated, and are projected to

increase due to increased agricultural operations to feed a growing world population (Reis et al., 2009; Ellis et al., 2013). Satellite observations showed that gas-phase NH_3 concentrations have increased substantially in US agricultural areas from 2002 to 2014 (Warner et al., 2017). More wildfires from a changing climate, or from controlled burning for land clearing for agricultural use, may also lead to increased NH_3 emissions (Reis et al., 2009; Pechony and Shindell, 2010; Warner et al., 2016). These trends suggest that NH_3 could play an increasingly important role in atmospheric chemistry.

Previous laboratory studies have shown that NH_3 can influence secondary organic aerosol (SOA) formation and processing. For example, NH_3 increases SOA mass yields in the α -pinene ozonolysis system, and is hypothesized to be due to the formation of ammonium salts from the reaction of NH_3 with organic acids (Na et al., 2007). The heterogeneous uptake of NH_3 by SOA can also lead to the formation of particulate organonitrogen compounds, a class of brown carbon species that can reduce visibility and impact climate (Laskin et al., 2010; Updyke et al., 2012; Lee et al., 2013; Laskin et al., 2015).

The southeastern U.S. is a natural outdoor laboratory for studying the effects of biogenic-anthropogenic interactions on atmospheric aerosol formation and processing. Subtropical vegetation composed mainly of mixed conifer and deciduous forests emit large quantities of biogenic volatile organic compounds (BVOCs) that can act as precursors for SOA formation (Blanchard et al., 2011; Guenther et al., 2012; Blanchard et al., 2013a). Large urban centers and small towns are surrounded by large expanses of forests and widespread rural areas with agricultural activities. Scattered within the southeastern U.S. are also coal-burning power plants and industrial facilities. Anthropogenic activities in this region emit large concentrations of VOCs, SO_2 , NO_x , CO, NH_3 and aerosols (Blanchard et al., 2013c). Similar to other parts of the U.S., SO_2 , CO and NO_x concentrations have decreased steadily in the southeastern U.S. due to the implementation of emission controls (Blanchard et al., 2013b). In contrast, gas-phase NH_3 concentrations have increased in the southeastern U.S. over the same time period (Saylor et al., 2015). These factors make the southeastern U.S. an intriguing place to study the influence of NH_3 on atmospheric aerosol chemistry.

We performed aerosol and gas measurements during a field study conducted in Yorkville, Georgia, U.S., in the fall of 2016, with the goal of understanding how NH_3 affects aerosol acidity

and SOA formation. The field site is surrounded by forest and agricultural land, affording an opportunity to make ambient observations in an area impacted by local emissions of BVOCs and NH_3 . In this paper, we present gas and aerosol composition measurements that includes a suite of organic acids. The thermodynamic equilibrium model, ISORROPIA-II, is used to calculate particle water and pH based on measured inorganic aerosol and gas composition (Nenes et al., 1998; Fountoukis and Nenes, 2007), and these predictions are compared to observed gas-particle partitioning of NH_3 , HNO_3 and organic acids. Together, these measurements are used to determine how aerosol acidity affects the mass concentration of particle-phase organic acids at this site.

2. Methods

2.1. Field site

Aerosol and gas measurements were conducted at the Yorkville, Georgia (33.929 N, 85.046 W) SouthEastern Aerosol Research and Characterization (SEARCH) field site from mid-August to mid-October 2016. This is one of the sampling sites for the Southeastern Center for Air Pollution and Epidemiology (SCAPE) study where aerosol characterization measurements were conducted in the summer and winter of 2012 (Xu et al., 2015a; Xu et al., 2015b). A detailed description of the field site can be found in Hansen et al. (2003). This rural site is situated in a mixed forest-agriculture area approximately 55 km northwest and generally upwind of Atlanta. The immediate surrounding area is used for cattle grazing and poultry concentrated animal feeding operations (CAFOs) (Fig. S1). There are no major roads near the field site and nearby traffic emissions were negligible. A large coal-fired power plant (Plant Bowen) is situated approximately 25 km north of the site. Hence, the field site is impacted mainly by BVOC and NH_3 emissions, with occasional spikes in SO_2 and minimal influence from urban anthropogenic pollutants such as HNO_3 , O_3 , NO_x and CO (Fig. S2). The sampling period was characterized by moderate temperatures (24.0 °C average, 32.6 °C max, 9.5 °C min) and high relative humidities (68.9 % RH average, 100 % RH max, 21.6 % RH min). Meteorological data are shown in Fig. S3. Data reported are displayed in eastern daylight time (EDT).

2.2. Instrumentation

Instruments were housed in a temperature controlled (~20 °C) trailer during the field study. Gas-phase HNO_3 , SO_2 and organic acids (formic, acetic, oxalic, butyric, glycolic, propionic,

valeric, malonic and succinic acids) were measured by a custom-built chemical ionization mass spectrometer (CIMS) using sulfur hexafluoride ions (SF_6^-) as reagent ions. SO_2 and HNO_3 were detected as fluoride adducts (F_2SO_2^- and $\text{NO}_3^- \cdot \text{HF}$, respectively) while the organic acids (HX) were detected primarily as conjugated anions (X^-) by the quadrupole mass spectrometer (Huey et al., 1995; Huey et al., 2004; Nah et al., 2018). This CIMS is referred hereafter as the SF_6 -CIMS. Gas-phase NH_3 was measured by an additional custom-built CIMS using protonated ethanol clusters ($(\text{C}_2\text{H}_5\text{OH})_n^+$) as reagent ions. NH_3 was detected primarily as NH_4^+ ions by the quadrupole mass spectrometer (Nowak et al., 2002; Yu and Lee, 2012; You et al., 2014a). This CIMS is referred hereafter as the NH_3 -CIMS.

Since HNO_3 , NH_3 and organic acids may condense on surfaces, both SF_6 -CIMS and NH_3 -CIMS used inlet configurations that minimized wall interactions (Huey et al., 2004; Nowak et al., 2006). Each CIMS was connected to an inlet (a 7.6 cm ID aluminum pipe) that protruded beyond the trailer's wall by ~ 40 cm into the ambient air. Both inlets were ~ 2 m above the ground. A donut-shaped ring was attached to the ambient sampling port of each pipe to curtail the influence of crosswinds on the pipe's flow dynamics. Both rings were wrapped with a fine wire mesh to prevent ingestion of insects. A flow of $\sim 2800 \text{ L min}^{-1}$ was maintained in each pipe using regenerative blowers (AMETEK Windjammer 116637-03). Part of this flow (7 L min^{-1} for the SF_6 -CIMS and 4.6 L min^{-1} for the NH_3 -CIMS) was sampled through a custom-made three-way PFA Teflon valve, which connected the pipe's center to the CIMS sampling orifice and could be switched automatically between ambient and background measurements.

Background measurements were performed every 25 min for 4 min for both the SF_6 -CIMS and NH_3 -CIMS. During each background measurement, the sampled air flow was passed through an activated charcoal scrubber (Sigma Aldrich) that removed SO_2 , HNO_3 and organic acids prior to delivery into the SF_6 -CIMS, and through a silicon phosphate scrubber (Perma Pure Inc.) that removed NH_3 prior to delivery into the NH_3 -CIMS. $> 99 \%$ of the targeted species were removed during background measurements for both the SF_6 -CIMS and NH_3 -CIMS. Standard addition calibrations were performed every 5 h for the SF_6 -CIMS using the outputs of a $1.12 \text{ ppm } ^{34}\text{SO}_2$ gas cylinder (Scott-Marrin Inc.) and a formic or acetic acid permeation device (VICI Metronics). Calibrations for the other gases measured by the SF_6 -CIMS were performed in post-field laboratory work, details of which can be found in Nah et al. (2018) and SI section S1. Standard

addition calibrations were performed hourly for the NH₃-CIMS using the output of a NH₃ permeation device (KIN-TEK). The outputs of the formic and acetic acid permeation devices were measured periodically by scrubbing the output of the permeation tube in deionized water, followed by ion chromatography analysis for formate and acetate. The emission rate of the NH₃ permeation device was measured using UV optical absorption (Neuman et al., 2003).

The detection limits for species measured by the SF₆-CIMS and NH₃-CIMS were approximated from 3 times the standard deviation values (3σ) of the ion signals measured during background mode. The detection limits for HNO₃, SO₂ and the various organic acids measured by the SF₆-CIMS ranged from 1 to 60 ppt for 2.5 min integration periods, which corresponded to the length of a background measurement with a ~4 % duty cycle for each m/z (Table S1). Measurement uncertainties for the concentrations of HNO₃, SO₂ and the various organic acids originate mainly from calibration measurements, and were between 12 and 25 % (Table S1). The detection limit for NH₃ measured by the NH₃-CIMS was 1 ppb for 2.3 min integration periods, which corresponded to the length of a background measurement with a ~29 % duty cycle for the NH₄⁺ ion. Measurement uncertainties for NH₃ concentrations were 13 %.

A high-resolution time-of-flight aerosol mass spectrometer (HR-ToF-AMS, Aerodyne Research Inc.) was used to measure the elemental composition of ambient non-refractory PM₁ (particles with aerodynamic diameters < 1 μ m). Ambient air was sampled at 16.7 L min⁻¹ through a URG PM₁ cyclone and then through a nafion dryer prior to delivery into the HR-ToF-AMS. Aerosols were dried to RH < 20 % to eliminate the influence of RH on the HR-ToF-AMS's particle collection efficiency. A detailed description of the HR-ToF-AMS can be found in the literature (DeCarlo et al., 2006; Canagaratna et al., 2007; Canagaratna et al., 2015). Briefly, the aerodynamic lens of the HR-ToF-AMS focused the dried submicron aerosols into a narrow beam. The aerosols were then impacted onto a heated tungsten surface (~600 °C) where they were flash vaporized. The resulting vapors were ionized by electron impact ionization (70 eV), and the ions were detected by a time-of-flight mass spectrometer. Gas-phase interferences were accounted for by subtracting the signals obtained during daily measurements of filtered, particle-free sampling air. Ionization efficiency calibrations were performed weekly using 300 nm ammonium nitrate and ammonium sulfate particles. Composition-dependent collection efficiency (CDCE) values of 0.44 to 0.55 were determined using the procedure detailed by Middlebrook et al. (2012), where CDCE

values are derived based largely on aerosol inorganic species concentrations and the relative humidity in the sampling line. In addition, a constant collection efficiency (CE) value of 0.9 was determined from the comparison of raw HR-ToF-AMS SO_4^{2-} data with other particulate SO_4^{2-} measurements performed during the study. Comparisons of aerosol mass concentrations obtained from the application of CDCE values (i.e., 0.44 to 0.55) vs. a constant CE value (i.e., 0.9) to the raw HR-ToF-AMS data are discussed in section 3.2. Uncertainties in HR-ToF-AMS measurements were estimated to be approximately 25 % (Canagaratna et al., 2007).

Particle-phase water-soluble organic acids, inorganic cations and anions were measured using two Particle-into-Liquid Sampler (PILS) systems coupled to ion chromatographs (ICs) (Orsini et al., 2003). Each PILS sampled ambient air at nominally 16.7 L min^{-1} through a URG PM_{10} cyclone. Before PILS1, which was used to measure water-soluble inorganic cation and anions, two long (24 cm) URG glass annular denuders coated with sodium carbonate and phosphorous acid were used to remove acidic and basic gases. Before PILS2, which measured water-soluble organic acids, a 28 cm parallel plate carbon denuder (Sunset Lab) was used to remove organic gases (Eatough et al., 1993). In each PILS, aerosols were mixed with water vapor at $\sim 100^\circ\text{C}$ generated from heated ultrapure deionized water (Weber et al., 2001; Orsini et al., 2003). The resulting droplets were impacted onto a plate, with the resulting liquid sample analyzed by ICs. Each IC system was calibrated at the beginning and end of the study using five multi-compound standards in order to create calibration curves. Periodically, a HEPA filter (Pall Life Sciences) was placed on the inlet to determine the background in near real-time. The measurement uncertainty for each IC system was about 10 %.

PILS1 was connected to two Dionex ICS-1500 ICs (Thermo Fisher Scientific) to measure the water-soluble inorganic ions. These two IC systems include an isocratic pump, self-regenerating anion or cation suppressor, and conductivity detector. This system will be referred hereafter as the PILS-IC. Anions were separated using a Dionex IonPac AS15 guard and analytical column (4 x 250 mm, Thermo Fisher Scientific) employing an eluent of 38 mM sodium hydroxide at a flow rate of 1.5 mL min^{-1} . Cations were separated using a Dionex IonPac CS12A guard and analytical column (4 x 250 mm, Thermo Fisher Scientific) employing an eluent of 18 mM methanesulfonic acid at a flow rate of 1 mL min^{-1} . A new chromatogram was obtained every 30

min with a sample loop fill time (i.e., ambient sample integration time) of 20 min. The limit of detection for the various anions and cations was approximately $0.01 \mu\text{g m}^{-3}$.

PILS2 was coupled to a Dionex ICS-4000 capillary high-pressure ion chromatography (HPIC) system to measure the water-soluble organic acids. The HPIC includes an eluent generator, isocratic pump, degasser, suppressor, carbonate removal device, and conductivity detector. This system will be referred hereafter as the PILS-HPIC. The organic acids were separated using a Dionex AS11-HC- $4\mu\text{m}$ capillary guard and analytical column ($0.4 \times 250\text{mm}$, Thermo Fisher Scientific), which used a potassium hydroxide gradient separation method at a flow rate of $0.015 \text{ mL min}^{-1}$. A new chromatogram was obtained every 60 min with a sample loop fill time of 2 min. The limit of detection for the various organic acids was approximately $0.001 \mu\text{g m}^{-3}$.

Particle- and gas-phase water-soluble organic carbon (WSOC_p and WSOC_g , respectively) were measured using two Sievers 900 series total organic carbon (TOC) analyzers (GE Analytical Instruments), as described by Sullivan et al. (2004). For WSOC_p measurements, ambient air was sampled at 15.2 L min^{-1} through a URG PM_{10} cyclone and a parallel plate carbon denuder into a PILS coupled to the first TOC analyzer. For WSOC_g measurements, ambient air was sampled at 20 L min^{-1} through a Teflon filter (45 mm diameter, $2.0 \mu\text{m}$ pore size, Pall Life Sciences) to remove particles in the air stream. This filter was changed every 3 to 4 days. The particle-free air was then directed to a MIST chamber filled with ultrapure deionized water, which scrubbed the soluble gases at an air flow rate of 20 L min^{-1} . Soluble gases with Henry's law constants greater than $10^3 \text{ mole L}^{-1} \text{ atm}^{-1}$ were scrubbed into deionized water in the MIST chamber (Spaulding et al., 2002). The resulting MIST chamber liquid sample was analyzed by the second TOC analyzer. The TOC analyzers converted the organic carbon in the liquid samples to carbon dioxide using UV radiation and chemical oxidation. The carbon dioxide formed was then measured by conductivity. The amount of organic carbon in the liquid samples is proportional to the measured increase in conductivity of the dissolved carbon dioxide. Each WSOC_p and WSOC_g measurement lasted 4 min. Background WSOC_p and WSOC_g measurements were performed for 45 min every 12 h by stopping the sample air flow and rinsing the system with deionized water. Both TOC analyzers were calibrated at the beginning and end of the study using varying concentrations of sucrose solutions to create calibration curves (as specified by the instrument manual). The limit of detections for WSOC_p and WSOC_g were 0.2 and $0.4 \mu\text{gC m}^{-3}$, respectively. The measurement

uncertainties for WSOC_p and WSOC_g were estimated to be 10 % based on uncertainties in the TOC analyzer, sample air and liquid flows.

A suite of instruments operated by the SEARCH network provided supporting gas and aerosol measurements (Hansen et al., 2003; Edgerton et al., 2005, 2006). O₃ was measured by a UV absorption instrument (Thermo Fisher Scientific) with a temporal resolution of 1 min. NO and NO_x were measured by a chemiluminescence instrument (Thermo Fisher Scientific) with a temporal resolution of 1 min. NO₂ was obtained from the difference between NO and NO_x. CO was measured by a non-dispersive infrared absorption instrument (Thermo Fisher Scientific) with a temporal resolution of 1 min. NH₃ was measured by a denuder-based instrument (ARA) with a temporal resolution of 5 min. Comparisons of measurements by the NH₃-CIMS and denuder-based instrument will be presented in section 3.1. A filter-based particle composition monitor (ARA) provided 24 h-integrated PM_{2.5} measurements of particle mass and major inorganic ions measured offline by ion chromatography. Organic carbon (OC) and elemental carbon (EC) in PM_{2.5} were measured by a OCEC Analyzer (Sunset Labs) with a temporal resolution of 1 h. This analyzer determined OC by thermal optical transmittance. VOCs were measured by a gas chromatography-flame ionization detector (GC-FID, Agilent Technologies) with a temporal resolution of 1h.

2.2. Particle pH and water calculation

The thermodynamic equilibrium model ISORROPIA-II was used to determine the phase state and composition of an NH₄⁺-SO₄²⁻-NO₃⁻-Cl⁻-Na⁺-Ca²⁺-K⁺-Mg²⁺-water inorganic aerosol in equilibrium with its corresponding gas-phase species (Fountoukis and Nenes, 2007; Nenes et al., 1998). This approach was used in previous studies to determine particle water and pH in different parts of the world (Guo et al., 2015; Bougiatioti et al., 2016; Guo et al., 2016; Weber et al., 2016; Guo et al., 2017a; Guo et al., 2017c; Shi et al., 2017). The pH of an aqueous solution is defined as the negative logarithm of the hydronium ion (H₃O⁺) activity on a molality basis (www.goldbook.iupac.org/html/P/P04524.html, last access: 6 July 2018):

$$pH = -\log_{10}[a(H^+)] = -\log_{10}[m(H^+)\gamma_m(H^+)/m^\theta] \quad (1a)$$

where $a(H^+)$ is the hydronium ion activity in an aqueous solution, $m(H^+)$ is the hydronium ion molality, $\gamma_m(H^+)$ is the molality-based hydronium ion activity coefficient, and m^θ is the standard molality (1 mol kg⁻¹). For simplicity, H₃O⁺ is denoted here as H⁺ even though we recognize that

the unhydrated hydrogen ion is rare in aqueous solutions. Since most thermodynamic equilibrium models (e.g., ISORROPIA-II, E-AIM) do not report liquid concentrations, but instead report species in terms of concentration per volume of air (e.g., $\mu\text{g m}^{-3}$, $\mu\text{mol m}^{-3}$), we have calculated the particle pH by:

$$pH = -\log_{10} \gamma_{H^+} H_{aq}^+ = -\log_{10} \frac{1000 \gamma_{H^+} H_{air}^+}{W_i + W_o} \cong -\log_{10} \frac{1000 \gamma_{H^+} H_{air}^+}{W_i} \quad (1b)$$

where γ_{H^+} is the hydronium ion activity coefficient (assumed to be 1), H_{aq}^+ is the concentration of hydronium ions in particle water in mole L^{-1} (i.e., the density of water is assumed to be 1000 kg m^{-3} , and so pH is calculated in terms of molality), H_{air}^+ ($\mu\text{g m}^{-3}$) is the hydronium ion concentration per volume of air, and W_i and W_o ($\mu\text{g m}^{-3}$) are the bulk particle water concentrations associated with inorganic and organic species per volume of air, respectively. In equation 1b, the molecular weight of H^+ is taken as 1 g mole^{-1} , and 1000 is the factor needed for unit conversion of g L^{-1} to $\mu\text{g m}^{-3}$. H_{air}^+ and W_i are outputs of the ISORROPIA-II model. Previous studies have shown that particle pH values predicted using only W_i are reasonably accurate since the sensitivity of particle pH to the effects of W_o is small (Guo et al., 2015). For the southeastern U.S., Guo et al. (2015) reported that particle pH values predicted using only W_i were systematically 0.15 to 0.23 units lower than those predicted using $W_i + W_o$ during the 2013 Southern Oxidant Aerosol Study (SOAS) and SCAPE campaigns. Given this small deviation and that organic aerosol hygroscopicity was not measured in this field study, we report particle pH only considering W_i .

ISORROPIA-II was run in “forward” mode, which assumes that aerosols are “metastable” with no solid precipitates, to predict particle pH and the partitioning of semi-volatile compounds. In “forward” mode, the model calculates the gas-particle equilibrium partitioning concentrations based on the input of the total concentration of a species (i.e., gas + particle). In “reverse” mode, the model calculates the gas-particle equilibrium partitioning concentrations based on the input of only the particle-phase concentration of a species. We used “forward” mode because the “reverse” mode is sensitive to measurement errors, which often result in large model biases in the predicted particle pH (Hennigan et al., 2015). The measured particle-phase inorganic NH_4^+ , SO_4^{2-} and NO_3^- concentrations and gas-phase HNO_3 and NH_3 concentrations were used as model inputs. The “metastable” assumption is reasonable since the high RH (average RH 68.9 %) observed during the study indicated that the aerosols had likely deliquesced. We excluded data for periods where

the RH was above 95 % since the exponential growth in particle liquid water with RH introduces large pH uncertainties (Malm and Day, 2001; Guo et al., 2015).

In using ISORROPIA-II to predict particle pH and the partitioning of semi-volatile compounds, we also assumed that the aerosols are internally mixed and that the particle pH does not change with particle size (i.e., the overall particle pH is characterized by the particle's bulk properties). As long as some small fraction of sulfate is mixed with various aerosol components, (e.g., non-volatile cations), the assumption that aerosols are completely internally mixed has a small effect on the predicted pH (Guo et al., 2017b). However, the presence of multiple organic and inorganic species in ambient aerosols may lead to multiple phases within the particle (i.e., phase separation). Consequently, this may result in the unequal distribution of inorganic species among different phases, each with its own water activity and inorganic concentration. Previous studies have shown that liquid-liquid and solid-liquid phase separations may occur for mixed organic and inorganic aerosols at low RH and organic aerosol oxygen-to-carbon atomic ratios (O/C) (Bertram et al., 2011; Song et al., 2012; You et al., 2013; You et al., 2014b; You and Bertram, 2015). Phase separations were always observed at $O/C \leq 0.5$, while no phase separation was observed at $O/C \geq 0.8$. The probability for the occurrence of phase separation decreased at higher RH for $0.5 < O/C < 0.8$. The average O/C for this field study is 0.69 ± 0.06 . Organic acids were not included in the calculation of particle pH. This is reasonable since their total mass concentration was small compared to the total inorganic mass concentration. The average ratio of the organic acid mass concentration to the inorganic mass concentration is 0.25. Furthermore, Song et al. (2018) showed that including organic acid mass concentrations in thermodynamic model calculations had minor effects on particle pH if the system is in equilibrium. The validity of these assumptions and the resulting thermodynamic model predictions will be evaluated by comparing the predicted gas-particle partitioning ratios of semi-volatile inorganic compounds with measured values in section 3.3.

3. Results and Discussion

3.1. NH₃ observations

Continuous measurements of NH₃ were made using the NH₃-CIMS from 13 September to 12 October. Figures 1a and 1b show the time series and average diurnal profile of NH₃,

respectively. NH_3 concentrations ranged from 0.7 to 39.0 ppb (0.5 to $28.5 \mu\text{g m}^{-3}$), and exhibited consistent diurnal cycles. NH_3 was generally higher in the late mornings and early afternoons. Concentrations started to increase at 07:30, which coincided with an increase in temperature at sunrise (Fig. S3). Possible reasons for the morning increase include volatilization of particulate ammonium and animal waste, entrainment from the residual layer where NH_3 may not have been depleted, evaporation of dew or fog that contained dissolved NH_3 , and emission from plant stomata (Ellis et al., 2011). NH_3 decreased at 14:30, approximately 1 hour before temperature decreased, and may be due to changes in the boundary layer height. However, this hypothesis cannot be tested since the boundary layer height was not measured during the study. The diurnal plot does not account for dilution as the boundary layer expanded, and only indicates that if emissions were solely from the surface and lower concentrations aloft, these NH_3 sources were of significant magnitude.

The average NH_3 concentration measured by the NH_3 -CIMS is 8.1 ± 5.2 ppb. This is approximately 2 times higher than the average NH_3 concentration (3.8 ± 2.9 ppb) measured by the denuder-based instrument operated by the SEARCH network over the same time period (Fig. S4). Differences in NH_3 concentrations measured by the two instruments may be due to positive and negative sampling artifacts caused by differences in sampling inlets (e.g., inlet length and location), frequency of calibration and background measurements, and (in the case of the denuder-based instrument) possible sample contamination during chemical analysis. Discussions on how differences in measured NH_3 concentrations affect PM_{10} pH predictions will be presented in section 3.3. Nevertheless, there is a record of NH_3 concentrations measured by the denuder-based instrument at this site since 2008. Just prior to, and during this study, NH_3 concentrations are generally the highest observed since 2011 (Fig. S5). These elevated NH_3 concentrations may be due to sporadic biomass burning episodes caused by elevated temperatures and widespread drought across the southeastern U.S. in 2016 (Park Williams et al., 2017; Case and Zavodsky, 2018).

The NH_3 -CIMS measurements are examined with the meteorological data to gain insights on the primary NH_3 sources during the sampling period. To account for wind speed, the 1-hour averaged NH_3 concentrations are first multiplied by their corresponding 1-hour averaged wind speeds. These normalized NH_3 concentrations are then used to construct a wind direction polar

plot showing the average normalized NH_3 concentration per 10 degrees bin (Fig. 1c). The wind direction polar plot shows that the normalized NH_3 is approximately 2 times greater than the average when air masses are transported from the south-east, the general direction of the poultry CAFOs located approximately 2 km from the field site (Fig. S1), which are known for high NH_3 emissions. This conclusion is reaffirmed by NH_3 measurements by the SEARCH network's denuder-based instrument.

NH_3 concentrations measured by the two instruments in this study are substantially higher than those measured in three recent field studies conducted in the continental U.S.: 2010 California Nexus (CalNex) study, 2013 Southeast Nexus (SENEX) study and 2013 SOAS study (see Table 1). The differences in NH_3 may be attributed to differences in land use, proximity to CAFOs and meteorological conditions. The high NH_3 concentrations in this study allow us to make ambient observations of the effect of NH_3 on particle acidity and the gas-particle partitioning of semi-volatile inorganic and organic compounds, and compare them with previous studies.

3.2. PM_{10} composition

The aerosol inorganic chemical composition was measured by several instruments during this study. The HR-ToF-AMS, PILS-IC and PILS-HPIC measured the composition of PM_{10} , while a filter-based particle composition monitor measured the composition of $\text{PM}_{2.5}$. Comparisons of aerosol SO_4^{2-} , NO_3^- and NH_4^+ mass concentrations obtained from the application of CDCE values to the raw HR-ToF-AMS data are compared to those measured by the other three instruments in Fig. S6. NH_4^+ measurements by the PILS-IC are not available for comparison due to denuder breakthrough that occurred during the study.

SO_4^{2-} measurements by the various instruments are generally well correlated with each other, with R^2 values ranging from 0.64 to 0.92. Although PM_{10} SO_4^{2-} measurements by the two PILS systems show good agreement with each other, HR-ToF-AMS CDCE-applied SO_4^{2-} measurements are approximately two times higher than the PILS and filter measurements. Similar systematic differences are also observed for NO_3^- and NH_4^+ measurements. NO_3^- and NH_4^+ measurements by the four instruments are moderately correlated ($R^2 = 0.54$ to 0.79 and $R^2 = 0.94$, respectively). NO_3^- measurements by the PILS and filter systems are mostly similar; however, HR-ToF-AMS CDCE-applied PM_{10} NO_3^- and NH_4^+ measurements are approximately three times and

two times higher than the PILS and filter measurements. One possible reason is that the calculated CDCE is lower due to organics dominating the aerosol composition during the study (average of 74.2 ± 7.9 % of the non-refractory PM_{10} mass concentration). Lee et al. (2015) suggested that a high organic mass fraction may impede the complete efflorescence of aerosols when they are passed through the drier prior to delivery into the HR-ToF-AMS, thus reducing the particle bounce and increasing the CE value. Hence, we estimated HR-ToF-AMS PM_{10} mass concentrations that would be consistent with PILS and filter measurements by multiplying all the raw HR-ToF-AMS data by a constant CE value of 0.9, which was obtained from comparisons of the raw HR-ToF-AMS SO_4^{2-} data with PILS-IC and PILS-HPIC SO_4^{2-} measurements. The constant CE-applied HR-ToF-AMS data is used in all our subsequent analyses.

Figure 2 shows the time series and average diurnal profiles of non-refractory PM_{10} species. The average non-refractory PM_{10} organics, SO_4^{2-} , NO_3^- and NH_4^+ mass concentrations are 5.0 ± 2.3 , 1.6 ± 0.4 , 0.2 ± 0.1 and $0.4 \pm 0.2 \mu\text{g m}^{-3}$, respectively. Organics are the dominant non-refractory PM_{10} species, accounting for 74.2 ± 7.9 % of the non-refractory PM_{10} mass concentration during the field study. Organic aerosol mass concentration was slightly higher at night, which is likely caused by changes in the boundary layer height, emission sources and SOA formation processes (Xu et al., 2015b). Previous studies have shown that nighttime SOA production in the Southeastern U.S. is largely attributed to nitrate radical oxidation and ozonolysis of monoterpenes, which are abundant at night (Pye et al., 2015; Xu et al., 2015a; Xu et al., 2015b; Lee et al., 2016; Zhang et al., 2018). Specifically, the nitrate radical oxidation of some monoterpenes (e.g., β -pinene) could form low volatility organic nitrates that are condensable and could contribute substantially to the nocturnal organic aerosol mass (Boyd et al., 2015; Boyd et al., 2017; Ng et al., 2017). Apportionment of organic aerosol sources will be discussed in an upcoming publication. SO_4^{2-} is the second most abundant non-refractory PM_{10} species (16.3 ± 5.7 % mass fraction), followed by NH_4^+ (5.9 ± 2 % mass fraction) and NO_3^- (3.6 ± 2.2 % mass fraction). SO_4^{2-} mass concentration peaked in the afternoon due to enhanced SO_2 photooxidation (Weber et al., 2003). The NO_3^- mass concentration measured by the HR-ToF-AMS is the nitrate functional group (-ONO₂) present on organic and inorganic nitrates. Hence, the diurnal profile of the NO_3^- mass concentration in Fig. 2 has contributions from both organic and inorganic nitrates. The mass concentrations of organic and inorganic nitrates increased after sunset and peaked at sunrise (Fig. S7), likely due to the formation of organic nitrates from nighttime NO_3 chemistry and increased

gas-to-particle partitioning of organic and inorganic nitrates as temperature decreased (Xu et al., 2015a; Xu et al., 2015b). Quantification and characterization of organic nitrates based on HR-ToF-AMS and PILS-IC PM₁ NO₃⁻ measurements will be discussed in a future publication. NH₄⁺ mass concentration has moderate diurnal variations with marginally higher concentrations in the afternoon, likely due to the contrasting day/night phases of ammonium sulfate and ammonium nitrate formation. SO₄²⁻, NO₃⁻ and NH₄⁺ molar concentrations indicated that NH₄⁺ is mainly associated with SO₄²⁻ in PM₁.

3.3. PM₁ pH predictions

CIMS HNO₃ and NH₃ data, HR-ToF-AMS PM₁ SO₄²⁻ and NH₄⁺ data, PILS-IC PM₁ NO₃⁻ and non-volatile cation (Cl⁻, Na⁺, Ca²⁺, K⁺ and Mg²⁺) data, measured temperature and RH are used as ISORROPIA-II model inputs to predict PM₁ W_i and pH from 13 September to 6 October. Figure 3 shows the time series and average diurnal profiles of ISORROPIA-predicted PM₁ W_i and pH. PM₁ are highly acidic with pH values ranging from 0.9 to 3.8, and an average pH of 2.2 ± 0.6 . The average PM₁ pH was 2.5 ± 0.6 during periods where the NH₃ concentration was higher than 13.3 ppb (i.e., average NH₃ concentration + 1 standard deviation = $8.1 + 5.2 = 13.3$ ppb). The PM₁ pH values in this study are generally similar to those reported by Guo et al. (2015) at the same field site during winter 2012. Our observation that PM₁ are acidic despite the high NH₃ concentrations in this study is consistent with previous studies showing that particle pH has weak sensitivities to wide NH₃ and SO₄²⁻ mass concentration ranges due to pH buffering caused by the partitioning of NH₃ between the gas and particle phases (Weber et al., 2016; Guo et al., 2017c). This weak particle pH sensitivity also explains the small changes in PM₁ pH values (about 10 % lower, Fig. S8) when NH₃ measurements by the SEARCH network denuder-based instrument are used in ISORROPIA-II calculations (instead of NH₃-CIMS measurements).

PM₁ pH varied by approximately 1.4 units throughout the day. W_i has an average value of $1.6 \pm 1.7 \mu\text{g m}^{-3}$. PM₁ W_i and pH showed similar diurnal profiles, with both peaking in the mid-morning and reaching their minima in the mid-afternoon. These diurnal trends are consistent with those previously reported by Guo et al. (2015) for PM₁ measured during the summer and winter in different parts of the southeastern U.S. Also shown in Fig. 3b is the diurnal profile of H_{air}^+ , which peaked in the mid-afternoon. The W_i and H_{air}^+ maximum/minimum ratios are comparable (6.5 and

5.3, respectively), thus indicating that the diurnal variation in particle pH is driven by both W_i and H_{air}^+ .

The average PM₁ pH for this study is about 1 unit higher than those for the SENEX and SOAS campaigns (Table 1), and is likely due to the much higher abundance of NH₃ in this study. The average NH₃ mass concentration in this study is approximately 49 times and 15 times higher than those in the SENEX and SOAS campaigns, respectively. The average PM₁ pH for this study is similar to that for the CalNex campaign even though the average NH₃ mass concentration in this study is only approximately 4 times higher than that in the CalNex campaign (Guo et al., 2017a). This may be due, in part, to PM₁ SO₄²⁻ and NO₃⁻ mass concentrations at CalNex being approximately 2 times and 18 times larger than those of this study, respectively. Aerosol inorganic SO₄²⁻ and NO₃⁻ species are hygroscopic species. The much higher NO₃⁻ mass concentrations in the CalNex campaign (due, in part, to high NO_x emissions) increased particle W_i substantially, which diluted H⁺ and raised particle pH, resulting in more gas-to-particle partitioning of NO₃⁻, and eventually leading to pH levels similar to those observed in this study. This type of feedback does not happen in the southeastern U.S. where non-volatile SO₄²⁻ dominates the uptake of particle water. It is also possible that the higher RH and lower temperatures during the CalNex campaign (relative to this study) contributed to high particle W_i , which diluted H⁺ and raised particle pH levels similar to those observed in this study.

The validity of this study's thermodynamic model predictions is evaluated by comparing the predicted gas-particle partitioning ratios of semi-volatile inorganic compounds (i.e., NO₃⁻ and NH₄⁺) with measured values (Fig. S9). CIMS HNO₃ and NH₃ data, PILS-IC NO₃⁻ and HR-ToF-AMS NH₄⁺ data are used in this comparison. $\epsilon(\text{NO}_3^-)$ and $\epsilon(\text{NH}_4^+)$ are defined as the particle-phase molar concentration divided by the total molar concentration (gas + particle), i.e., $\epsilon(\text{NO}_3^-) = \text{NO}_3^- / (\text{HNO}_3 + \text{NO}_3^-)$ and $\epsilon(\text{NH}_4^+) = \text{NH}_4^+ / (\text{NH}_3 + \text{NH}_4^+)$. Predicted NH₃, NH₄⁺ and $\epsilon(\text{NH}_4^+)$ values are generally within 10 % of and are highly correlated ($R^2 = 0.96$ to 0.99) with measured values (Fig. S9). While predicted HNO₃ values generally agreed with measurements, substantial scatter can be seen between the predicted and measured values for NO₃⁻ and $\epsilon(\text{NO}_3^-)$. This scatter can be attributed, at least in part, to uncertainties brought about by the low PM₁ NO₃⁻ mass concentrations and effects of coarse mode cations (e.g., Na⁺, Ca²⁺, K⁺ and Mg²⁺) on fine mode HNO₃-NO₃⁻ gas-particle equilibrium (i.e., HNO₃ can partition to both fine and coarse modes, thereby affecting fine

mode NO_3^- concentrations; no such effect occurs for $\text{NH}_3\text{-NH}_4^+$ gas-particle equilibrium). In general, the overall good agreement between model predictions and measurements indicated that our assumptions that aerosols are metastable (i.e., aerosols are supersaturated aqueous droplets) with no phase separation for the thermodynamic calculations are reasonable for the conditions of this study, and do not affect model predictions.

The molar fractions of NO_3^- and NH_4^+ in the particle phase (i.e., $\varepsilon(\text{NO}_3^-)$ and $\varepsilon(\text{NH}_4^+)$) measured in this study are compared with those measured during the CalNex, SENEX and SOAS campaigns. Figure 4 shows the measured $\varepsilon(\text{NO}_3^-)$ and $\varepsilon(\text{NH}_4^+)$ values as a function of their ISORROPIA-predicted particle pH for the various field studies. For each field study, only a subset of the data is chosen for this comparison ($1 \leq W_i \leq 4 \mu\text{g m}^{-3}$ and $15 \text{ }^\circ\text{C} \leq \text{temperature} \leq 25 \text{ }^\circ\text{C}$) to reduce the effects of variability of W_i and temperature on gas-particle partitioning for comparison with the calculated S (or sigmoidal) curves, which are calculated based on $W_i = 2.5 \mu\text{g m}^{-3}$ and temperature = $20 \text{ }^\circ\text{C}$. The S curves for $\text{HNO}_3\text{-NO}_3^-$ and $\text{NH}_3\text{-NH}_4^+$ partitioning as a function of particle pH are also plotted as solid lines. The S curves are calculated based on the solubility and dissociation of NO_3^- and NH_4^+ species in water:

$$\varepsilon(\text{NO}_3^-) = \frac{H_{\text{HNO}_3}^* RTW_i \times 0.987 \times 10^{-14}}{\gamma_{\text{H}^+} \gamma_{\text{NO}_3^-} 10^{-\text{pH}} + H_{\text{HNO}_3}^* RTW_i \times 0.987 \times 10^{-14}} \quad (2)$$

$$\varepsilon(\text{NH}_4^+) = \frac{\frac{\gamma_{\text{H}^+} 10^{-\text{pH}}}{\gamma_{\text{NH}_4^+}} H_{\text{NH}_3}^* RTW_i \times 0.987 \times 10^{-14}}{1 + \frac{\gamma_{\text{H}^+} 10^{-\text{pH}}}{\gamma_{\text{NH}_4^+}} H_{\text{NH}_3}^* RTW_i \times 0.987 \times 10^{-14}} \quad (3)$$

where $H_{\text{HNO}_3}^*$ and $H_{\text{NH}_3}^*$ ($\text{mole}^2 \text{ kg}^{-2} \text{ atm}^{-1}$) are equilibrium constants and are the products of the Henry's law constant and the dissociation constant of HNO_3 and NH_3 , respectively, R is the gas constant ($8.314 \text{ m}^3 \text{ Pa K}^{-1} \text{ mol}^{-1}$), T is temperature (K), and γ_i 's are activity coefficients. $H_{\text{HNO}_3}^*$ and $H_{\text{NH}_3}^*$ values at $20 \text{ }^\circ\text{C}$ are calculated using equations found in Clegg and Brimblecombe (1990) and Clegg et al. (1998), respectively. Activity coefficients predicted by ISORROPIA-II are $\gamma_{\text{H}^+ - \text{NO}_3^-} = \sqrt{\gamma_{\text{H}^+} \gamma_{\text{NO}_3^-}} = 0.28$, $\gamma_{\text{H}^+} = 1$ and $\gamma_{\text{NH}_4^+} = 1$. Derivations of the analytically calculated S curves for $\varepsilon(\text{NO}_3^-)$ and $\varepsilon(\text{NH}_4^+)$ in equations 2 and 3 can be found in Guo et al. (2017a). As shown in Fig. 4, the measured $\varepsilon(\text{NO}_3^-)$ and $\varepsilon(\text{NH}_4^+)$ values for the four field studies all generally converged on the calculated S curves. The higher particle pH values in this study and the CalNex

campaign relative to those for the SENEX and SOAS campaigns resulted in less NH_3 and more HNO_3 partitioned to the particle phase, as predicted by these simple analytical expressions. A similar analysis will be performed for the organic acids in section 3.5.

3.4. WSOC and water-soluble organic acids

The time series and average diurnal profiles of WSOC_g and WSOC_p are shown in Fig. S10. The average WSOC_g mass concentration ($3.6 \pm 2.7 \mu\text{gC m}^{-3}$) is roughly four times higher than that of WSOC_p ($1.0 \pm 0.6 \mu\text{gC m}^{-3}$). The diurnal profile of WSOC_p is somewhat flat, likely due to various organic aerosol sources having different water solubility and diurnal cycles, and compensating each other throughout the day (Xu et al., 2015b; Xu et al., 2017). In contrast, WSOC_g displayed strong diurnal variations. WSOC_g increased at 07:30, which coincided with the sharp increase in solar irradiance (Fig. S3). WSOC_g decreased at 21:30, approximately 2 hours after sunset. Also shown in Fig. S10 are the time series and average diurnal profile of the mass fraction of total WSOC in the particle phase, i.e., $F_p = \text{WSOC}_p / (\text{WSOC}_p + \text{WSOC}_g)$. The peak F_p coincided with the minima of WSOC_g at 07:30.

The average WSOC_g and WSOC_p ($3.6 \pm 2.7 \mu\text{gC m}^{-3}$ and $1.0 \pm 0.6 \mu\text{gC m}^{-3}$) are slightly lower than those measured during the SOAS campaign (SOAS $\text{WSOC}_g = 4.9 \mu\text{gC m}^{-3}$ and $\text{WSOC}_p = 1.7 \mu\text{gC m}^{-3}$) (Xu et al., 2017). While the diurnal profiles of WSOC_p in both studies are flat, the diurnal profiles of WSOC_g measured in the two studies are different. WSOC_g measured in the SOAS study decreased at sunset, while WSOC_g measured in this study decreased 2 hours after sunset. Differences in WSOC_g diurnal profiles in the two studies are likely due to differences in emission sources as a result of different sampling periods (SOAS was in early summer and this study was in early fall), land use and/or land cover. The ratio of WSOC_p to OC for this study was estimated at 30 %, but this comparison is imprecise because WSOC_p was PM_{10} and OC was $\text{PM}_{2.5}$ (refer to Fig. S11 and SI section S2).

Figure 5 shows the time series of particle- and gas-phase concentrations of formic, acetic, oxalic, malonic, succinic, glutaric and maleic acids. Their diurnal profiles are shown in Fig. 6. Gas-phase measurements of glutaric and maleic acids are not available. Gas-phase measurements of butyric, glycolic, propionic and valeric acids were also measured during the study and have

been presented in Nah et al. (2018), but will not be discussed here since their particle-phase measurements are not available.

Assuming that all the measured organic acids are completely water-soluble, 30 % of the WSOC_g is comprised of these organic acids (Nah et al., 2018). Formic and acetic acids are the most abundant gas-phase organic acids, with averages of 2.2 ± 1.6 and $1.9 \pm 1.3 \mu\text{g m}^{-3}$, respectively. The average carbon mass fraction of WSOC_g comprised of formic and acetic acids are 7 and 13 %, respectively. All the gas-phase organic acids displayed strong and consistent diurnal cycles, with higher concentrations being measured during warm and sunny days. Their concentrations start to increase at sunrise (at 07:30), building to a peak between 15:30 and 19:30, then decrease overnight.

Nah et al. (2018) previously showed that the measured gas-phase organic acids during the study, including oxalic acid, likely have the same or similar sources. Poor correlations between gas-phase organic acid concentrations and those of anthropogenic pollutants (HNO₃, SO₂, CO and O₃) indicated that these organic acids are not due to anthropogenic emissions, and are likely biogenic in nature. Biogenic emissions of gas-phase organic acids and/or their BVOC precursors are elevated at high temperatures, resulting in higher organic acid concentrations during warm and sunny days. For example, isoprene, which is the dominant BVOC in Yorkville, has a somewhat similar diurnal profile as the organic acids. In addition, the concentration of isoprene is moderately correlated with those of formic and acetic acids (Fig. S10 of Nah et al., 2018), which are known products of isoprene photooxidation. Some of these gas-phase organic acids may also be formed in the particle phase during organic aerosol photochemical aging, with subsequent volatilization into the gas phase. The gas-particle partitioning of organic acids likely depends on thermodynamic conditions, which are controlled by particle pH and W_i and meteorological conditions as will be shown in section 3.5.

The measured particle-phase water-soluble organic acids contributed on average 6 % to the HR-ToF-AMS-measured organic aerosol mass concentration. The average carbon mass fraction of WSOC_p comprised of these organic acids is 4 %. Previous studies have shown that particle-phase organic acids found in rural environments are oxidation products of gas-phase aliphatic monocarboxylic acids, which are formed in the photochemical oxidation of biogenic unsaturated fatty acids and other BVOC precursors (Kawamura and Gagosian, 1987; Kawamura and Ikushima,

1993; Kerminen et al., 2000; Kawamura and Bikkina, 2016). These particle-phase organic acids can also be produced during the multiphase photochemical aging of ambient organic aerosols (Ervens et al., 2004; Lim et al., 2005; Sorooshian et al., 2007; Sorooshian et al., 2010).

Oxalate is the most abundant measured particle-phase water-soluble organic acid anion (contributing on average 26 % to the total particle-phase organic acid mass concentration), with mass concentrations ranging from 0.01 to 0.34 $\mu\text{g m}^{-3}$ and a average of $0.07 \pm 0.05 \mu\text{g m}^{-3}$. Acetate (average of $0.06 \pm 0.03 \mu\text{g m}^{-3}$) and formate (average of $0.05 \pm 0.03 \mu\text{g m}^{-3}$) are the second and third most abundant measured particle-phase water-soluble organic acid anions, respectively. Particle-phase formate, acetate and maleate showed weak diurnal variations, and may be due, in part, to various emission sources having different diurnal cycles and compensating each other throughout the day. Particle-phase oxalate, malonate and succinate peaked in the mid- to late afternoon, while glutarate generally peaked in the mid-morning. This suggests that while the production of these organic acids is photochemically-driven, they may have different BVOC precursors and/or different photochemical production pathways. In addition, since oxalic (C_2), malonic (C_3), succinic (C_4) and glutaric (C_5) acids belong to the same homologous series of organic diacids, it is possible that the photochemical aging of particle-phase glutaric acid resulted in the formation of its successive homologues via the cleavage of C-C bonds. Hence, organic aerosol photochemical aging may also have contributed to the diurnal profiles of particle-phase oxalate, malonate, succinate and glutarate.

3.5. Gas-particle partitioning of organic acids

The online and simultaneous measurements of gas- and particle-phase organic acid mass concentrations provided the opportunity to study gas-particle partitioning behavior of semi-volatile organic compounds with respect to particle pH, as is more commonly done with semi-volatile inorganic species (see section 3.3). Since formic, acetic and oxalic acids are the three most abundant measured organic acids present in the gas and particle phases, we focus on the gas-particle partitioning behaviors of these three organic acids. The average molar fractions (± 1 standard deviation) of formic, acetic and oxalic acid in the particle phase (i.e., $\epsilon(\text{HCOO}^-)$, $\epsilon(\text{CH}_3\text{CO}_2^-)$ and $\epsilon(\text{C}_2\text{O}_4^{2-})$) are $3.6 \pm 3.6 \%$, $5.8 \pm 5.0 \%$ and $73.7 \pm 9.8 \%$, respectively. The uncertainties of these ratios for formic, acetic and oxalic acids are 16, 16 and 17 %, respectively,

which are obtained from the propagation of their SF₆-CIMS and PILS-HPIC measurement uncertainties.

3.5.1. Oxalic acid

To investigate the factors affecting oxalic acid gas-particle partitioning, the equation for the S curve describing the dependence of oxalic acid gas-particle partitioning (i.e., $\epsilon(\text{C}_2\text{O}_4^{2-}) = \text{C}_2\text{O}_4^{2-} / (\text{C}_2\text{H}_2\text{O}_4 + \text{C}_2\text{O}_4^{2-})$) on particle pH is derived. As shown in SI section S3, the analytically calculated S curve for $\epsilon(\text{C}_2\text{O}_4^{2-})$ can be simplified to:

$$\epsilon(\text{C}_2\text{O}_4^{2-}) \cong \frac{H_{\text{C}_2\text{H}_2\text{O}_4} W_i RT \left(\frac{\gamma_H + \gamma_{\text{C}_2\text{HO}_4^-}}{\gamma_{\text{C}_2\text{H}_2\text{O}_4}} 10^{-\text{pH} + K_{a1}} \right) \times 0.987 \times 10^{-14}}{\gamma_H + \gamma_{\text{C}_2\text{HO}_4^-} 10^{-\text{pH}} + H_{\text{C}_2\text{H}_2\text{O}_4} W_i RT \left(\frac{\gamma_H + \gamma_{\text{C}_2\text{HO}_4^-}}{\gamma_{\text{C}_2\text{H}_2\text{O}_4}} 10^{-\text{pH} + K_{a1}} \right) \times 0.987 \times 10^{-14}} \quad (4)$$

where $H_{\text{C}_2\text{H}_2\text{O}_4}$ (mole L⁻¹ atm⁻¹) is the Henry's law constant for oxalic acid, K_{a1} (mole L⁻¹) is the first acid dissociation constant for oxalic acid, R is the gas constant (8.314 m³ Pa K⁻¹ mol⁻¹), T is temperature (K), and γ_i 's are activity coefficients. We used the web version of AIOMFAC (www.aiomfac.caltech.edu) (Zuend et al., 2008; Zuend et al., 2011; Zuend et al., 2012) to compute an average $\gamma_{\text{C}_2\text{H}_2\text{O}_4}$ value of 0.0492. Since AIOMFAC does not predict $\gamma_H + \gamma_{\text{C}_2\text{HO}_4^-}$, we assumed that $\gamma_H + \gamma_{\text{C}_2\text{HO}_4^-} = \gamma_H + \gamma_{\text{NO}_3^-}$, and used the ISORROPIA-predicted $\gamma_H + \gamma_{\text{NO}_3^-}$ value of 0.07. We used the average of $H_{\text{C}_2\text{H}_2\text{O}_4}$ values provided by Clegg et al. (1996), Compernelle and Muller (2014) and Saxena and Hildemann (1996) (6.11 x 10⁸ mole L⁻¹ atm⁻¹ at 25 °C), and accounted for the effect of temperature using equation 19 in Sander (2015). Although K_{a1} also depends on temperature, we used the K_{a1} value at 25 °C (5.62 x 10⁻² mole L⁻¹, (Haynes, 2014)) for all the oxalic acid S curve calculations since equations that compute K_{a1} values for pure aqueous oxalic acid solutions at different temperatures are not available in the literature. In addition, the temperatures observed in this study were close to 25 °C (study-average temperature = 23.4 ± 4.0 °C).

Different S curves for $\epsilon(\text{C}_2\text{O}_4^{2-})$ are calculated using 1-hour average values obtained from the diurnal profiles of temperature and W_i (specifically at 00:30, 06:30 and 12:30). The shape of the S curve changes with the time of day due to the diurnal variations of temperature and W_i (Fig S12 and SI section S3). The S curves for $\epsilon(\text{C}_2\text{O}_4^{2-})$ are very different from those of other acids,

such as $\varepsilon(\text{NO}_3^-)$ (shown in Fig. 4b). From the S curves for $\varepsilon(\text{C}_2\text{O}_4^{2-})$, which are calculated using conditions in this study, some molar fraction of oxalic acid is always expected to be present in the particle phase, even at low particle pH (i.e., the S curve does not go to zero at low pH). In contrast, HNO_3 is expected to be present primarily in the gas phase at low particle pH (i.e., $\text{pH} < 1$) under similar temperature and W_i conditions. This is due primarily to differences in the Henry's law constants for the two acids. H_{HNO_3} ($2.57 \times 10^5 \text{ mole L}^{-1} \text{ atm}^{-1}$) at 23.4°C is three orders of magnitude smaller than $H_{\text{C}_2\text{H}_2\text{O}_4}$ ($7.27 \times 10^8 \text{ mole L}^{-1} \text{ atm}^{-1}$) (Clegg and Brimblecombe, 1990; Sander, 2015). This means that some undissociated form of oxalate can be found in the particle phase at any pH, and the molar fraction of this form increases with particle W_i (see Fig. S12). Oxalic acid's very high Henry's law constant combined with the W_i conditions in this study ensures that some fraction of the organic acid will be in the particle phase regardless the particle pH.

Figure 7 compares the measured $\varepsilon(\text{C}_2\text{O}_4^{2-})$ vs. ISORROPIA-predicted PM_1 pH to the analytically calculated S curves(s). The S curve is calculated based on the average temperature and W_i from 13 September to 6 October ($23.4 \pm 4.0^\circ\text{C}$ and $1.6 \pm 1.7 \mu\text{g m}^{-3}$, respectively). We also calculated the “upper” and “lower” bounds of this S curve based on one standard deviation from the average temperature and average W_i . Temperature = 27.4°C and $W_i = 0.5 \mu\text{g m}^{-3}$ are used for calculations of the “lower” bound, while temperature = 19.4°C and $W_i = 3.3 \mu\text{g m}^{-3}$ are used for calculations of the “upper” bound. For the ambient data, a range in W_i (0.5 to $4 \mu\text{g m}^{-3}$) and temperature (15 to 31°C) is chosen to be close to the analytical calculation. As shown in Fig. 7, the measured $\varepsilon(\text{C}_2\text{O}_4^{2-})$ generally converged around the S curve calculated using the average temperature and W_i values. Although there is some scatter, the measured ratios are mostly within the “upper” and “lower” bounds of the S curve.

Since the measured $\varepsilon(\text{C}_2\text{O}_4^{2-})$ are in general agreement with the analytically calculated S curve (Fig. 7), we can use the S curve to understand qualitatively how high NH_3 events at the site affect oxalic acid gas-particle partitioning. Here we define high NH_3 events as periods where the NH_3 concentration was higher than 13.3 ppb (which is the average NH_3 concentration + 1 standard deviation). As discussed in section 3.3, the PM_1 pH during high NH_3 events is 2.5 ± 0.6 , which is slightly higher than the average PM_1 pH of 2.2 ± 0.6 . Based on the S curve calculated using the

average temperature and W_i values, $\epsilon(\text{C}_2\text{O}_4^{2-})$ increases from 81 % to 89 % when particle pH increases from 2.2 to 2.5. While this result indicates that high NH_3 concentrations can raise the particle pH sufficiently such that it can promote gas-to-particle partitioning of oxalic acid, this is not always the case. Specifically, increasing the particle pH from -2 (or lower) to 1 will not result in a significant increase in $\epsilon(\text{C}_2\text{O}_4^{2-})$. Therefore, whether or not particle pH, and consequently oxalic acid gas-particle partitioning, is sensitive to NH_3 concentration depends strongly on particle pH values.

We also examined how well the analytically calculated S curve for $\epsilon(\text{C}_2\text{O}_4^{2-})$ captures diurnal variations of the measured $\epsilon(\text{C}_2\text{O}_4^{2-})$. The ambient data is divided into two 12 hour sets (08:00 to 19:59 and 20:00 to 07:59) based on the diurnal profile of solar irradiance. Two S curves and their corresponding “upper” and “lower” bounds are calculated based on the average temperature and W_i of the two data sets, and are subsequently compared to the ambient data. As shown in Fig. S13, the measured $\epsilon(\text{C}_2\text{O}_4^{2-})$ in both data sets are generally consistent with predicted values.

A number of inferences can be drawn from the overall good agreement between the predicted and measured molar fractions of oxalic acid in the particle phase in Figs. 7 and S13. Our assumptions regarding the activity coefficients, Henry’s law constant and acid dissociation constants used in the S curve calculations of $\epsilon(\text{C}_2\text{O}_4^{2-})$ are reasonable for the conditions of this study (or are at least self-consistent). Analytically calculated S curves are a simple way of exploring how the gas-particle partitioning of semi-volatile inorganic and organic compounds in the atmosphere are affected by the compound’s physicochemical properties (e.g., Henry’s law constants and acid dissociation constants), temperature, W_i and pH. Overall, these results indicate that particle-phase oxalate is in equilibrium with gas-phase oxalic acid, and that particle pH can influence particle-phase oxalate concentrations. It also showed that particle-phase oxalate can be found over a broad pH range, and that the presence of oxalate does not necessarily provide insights of the particle pH. Because of its high Henry’s law constant, particle-phase oxalate can be found in aerosols even at extremely low pH values (i.e., the flat region in Fig. 7), although our data cannot be used to test this since ambient particle pH values in this study are too high.

3.5.2 Formic and acetic acids

Similar comparisons between the predicted and measured $\epsilon(\text{HCOO}^-)$ and $\epsilon(\text{CH}_3\text{CO}_2^-)$ can also be made. Derivation of the equations for S curves describing the dependence of formic and acetic acid gas-particle partitioning (i.e., $\epsilon(\text{HCOO}^-) = \text{HCOO}^- / (\text{HCOOH} + \text{HCOO}^-)$ and $\epsilon(\text{CH}_3\text{CO}_2^-) = \text{CH}_3\text{CO}_2^- / (\text{CH}_3\text{CO}_2\text{H} + \text{CH}_3\text{CO}_2^-)$, respectively) on particle pH are similar to that of HNO_3 since they are monoprotic acids:

$$\epsilon(\text{HCOO}^-) = \frac{H_{\text{HCOOH}} W_i R T \left(\frac{\gamma_H + \gamma_{\text{HCOO}^-}}{\gamma_{\text{HCOOH}}} 10^{-\text{pH} + K_{a1}} \right) \times 0.987 \times 10^{-14}}{\gamma_H + \gamma_{\text{HCOO}^-} 10^{-\text{pH}} + H_{\text{HCOOH}} W_i R T \left(\frac{\gamma_H + \gamma_{\text{HCOO}^-}}{\gamma_{\text{HCOOH}}} 10^{-\text{pH} + K_{a1}} \right) \times 0.987 \times 10^{-14}} \quad (5)$$

$$\epsilon(\text{CH}_3\text{CO}_2^-) = \frac{H_{\text{CH}_3\text{CO}_2\text{H}} W_i R T \left(\frac{\gamma_H + \gamma_{\text{CH}_3\text{CO}_2^-}}{\gamma_{\text{CH}_3\text{CO}_2\text{H}}} 10^{-\text{pH} + K_{a1}} \right) \times 0.987 \times 10^{-14}}{\gamma_H + \gamma_{\text{CH}_3\text{CO}_2^-} 10^{-\text{pH}} + H_{\text{CH}_3\text{CO}_2\text{H}} W_i R T \left(\frac{\gamma_H + \gamma_{\text{CH}_3\text{CO}_2^-}}{\gamma_{\text{CH}_3\text{CO}_2\text{H}}} 10^{-\text{pH} + K_{a1}} \right) \times 0.987 \times 10^{-14}} \quad (6)$$

where H_{HCOOH} and $H_{\text{CH}_3\text{CO}_2\text{H}}$ (mole $\text{L}^{-1} \text{atm}^{-1}$) are the Henry's law constants for formic and acetic acid, K_{a1} 's (mole L^{-1}) are the first acid dissociation constants, R is the gas constant ($8.314 \text{ m}^3 \text{ Pa K}^{-1} \text{ mol}^{-1}$), T is temperature (K), and γ_i 's are activity coefficients. We used the web version of AIOMFAC (www.aiomfac.caltech.edu) (Zuend et al., 2008; Zuend et al., 2011; Zuend et al., 2012) to compute average γ_{HCOOH} and $\gamma_{\text{CH}_3\text{CO}_2\text{H}}$ values of 0.334 and 2.150, respectively. Similar to the case of oxalic acid, we assumed that $\gamma_H + \gamma_{\text{HCOO}^-} = \gamma_H + \gamma_{\text{CH}_3\text{CO}_2^-} = \gamma_H + \gamma_{\text{NO}_3^-}$, and used the ISORROPIA-predicted $\gamma_H + \gamma_{\text{NO}_3^-}$ value of 0.07. Temperature-dependent H_{HCOOH} and $H_{\text{CH}_3\text{CO}_2\text{H}}$ values are obtained from Sander (2015) using the same methodology employed to determine temperature-dependent $H_{\text{C}_2\text{H}_2\text{O}_4}$ values. We used K_{a1} values at 25°C (1.78×10^{-4} mole L^{-1} for formic acid, and 1.75×10^{-5} mole L^{-1} for acetic acid (Haynes, 2014)) for the S curve calculations.

S curves for $\epsilon(\text{HCOO}^-)$ and $\epsilon(\text{CH}_3\text{CO}_2^-)$ calculated based on temperature = 23.4°C and $W_i = 1.6 \mu\text{g m}^{-3}$ can be seen in Fig. 8. Practically no formic or acetic acids are predicted to partition to the particle phase (relative to oxalic acid) for the range of PM_1 pH calculated in this study. This is due to significant differences in the Henry's law constants and acid dissociation constants for the three organic acids. H_{HCOOH} and $H_{\text{CH}_3\text{CO}_2\text{H}}$ (9540 and 5370 mole $\text{L}^{-1} \text{atm}^{-1}$, respectively) at 23.4°C are substantially smaller than $H_{\text{C}_2\text{H}_2\text{O}_4}$ (7.27×10^8 mole $\text{L}^{-1} \text{atm}^{-1}$) (Sander, 2015). The K_{a1} values for formic and acetic acids (1.78×10^{-4} and 1.75×10^{-5} mole L^{-1} , respectively) are also considerably smaller than the K_{a1} value for oxalic acid (5.62×10^{-2} mole L^{-1}) (Haynes, 2014). Note

that H_{HNO_3} is between that of $H_{C_2H_2O_4}$ and those of H_{HCOOH} and $H_{CH_3CO_2H}$ (compare Fig. 4b with Figs. 7 and 8).

As shown in Fig. 8, higher than expected levels of formate and acetate are observed in the particle phase. This has also been reported in previous studies (Liu et al., 2012). Laboratory tests showed that the disagreement cannot be explained by positive biases in the particle-phase formate and acetate PILS-HPIC measurements resulting from less than 100 % gas removal by the carbon denuder. The measured denuder efficiency for formic acid was $\geq 99.97\%$ (SI section S4). The possibility that formic and acetic acid dimers in the aqueous phase (Schrier et al., 1964; Gilson et al., 1997; Chen et al., 2008) may result in higher than predicted molar fractions of formate and acetate in the particle phase was explored, but also could not explain the observed gas-particle partitioning of these acids (SI section S5). The disagreement could be due to incorrect Henry's law constants for formic and acetic acids. However, the Henry's law constants for formic and acetic acid would have to be $\sim 10^4$ times and $\sim 3 \times 10^5$ times larger than their literature values, respectively, in order for their S curves to match our measured molar fractions of formic and acetic acid in the particle phase. In addition, formic and acetic acids may not be internally mixed with most of the other PM_1 aerosol components (e.g., SO_4^{2-} , NO_3^- , NH_4^+ , $C_2O_4^{2-}$), and thus are not associated with acidic aerosols, as assumed above. They may instead be associated with aerosols largely composed of non-volatile cations and have a pH closer to neutral. More research is needed to explain this disagreement.

4. Summary

Gas- and particle-phase measurements were conducted in Yorkville, Georgia (a rural field site) during fall 2016. The goal of the field study was to understand how NH_3 affects particle acidity, and consequently SOA formation through the gas-particle partitioning of semi-volatile inorganic and organic compounds. Since it is a rural site surrounded by forest, agricultural land and CAFOs, this study provided an opportunity for ambient observations in an area impacted by high local emissions of BVOCs and NH_3 .

NH_3 concentrations measured by the NH_3 -CIMS ranged from 0.7 to 39.0 ppb (average 8.1 ± 5.2 ppb), which were substantially higher than typical levels in the southeastern U.S.. PM_1 inorganic chemical composition, gas-phase HNO_3 and NH_3 concentrations, temperature and RH

were used as model inputs in the ISORROPIA-II thermodynamic model to calculate PM_1 pH and W_i . PM_1 pH ranged from 0.9 to 3.8, with an average pH of 2.2 ± 0.6 . The measured and predicted HNO_3 - NO_3^- and NH_3 - NH_4^+ gas-particle partitioning ratios were in good agreement. The measured gas-phase organic acids were estimated to contribute 30 % of the overall $WSOC_g$ on a carbon mass basis, whereas measured particle-phase organic acids comprised 6 % of the total organic aerosol mass concentration and 4 % of the overall $WSOC_p$ on a carbon mass basis. Formic and acetic acids were the most abundant gas-phase organic acids, with averages of 2.2 ± 1.6 and $1.9 \pm 1.3 \mu g m^{-3}$, respectively. Oxalate was the most abundant particle-phase water-soluble organic acid anion, with a average of $0.07 \pm 0.05 \mu g m^{-3}$. Measured oxalic acid gas-particle partitioning ratios generally agreed with analytical predictions, which were based on oxalic acid's physicochemical properties (specifically, its Henry's law constants, acid dissociation constants and activity coefficients), temperature, W_i and particle pH. The partitioning of oxalic acid to the particle phase is highly sensitive to temperature and W_i . In contrast, the partitioning of formic and acetic acids to the particle phase were higher than predicted for reasons currently unknown.

Although past air regulations have resulted in decreased sulfate, nitrate and ammonium aerosol mass concentrations across the U.S., our study suggests that the current limited regulation of NH_3 emissions may result in some increase in the organic aerosol mass concentration due to increased gas-to-particle partitioning of some organic acids. However, in this study, the effect was small since the organic acids comprised a small fraction of the overall organic aerosol mass.

5. Acknowledgements

The authors thank Eric Edgerton (Atmospheric Research and Analysis, Inc.) for providing SEARCH network measurements and meteorological data.

6. Funding

This publication was developed under U.S. Environmental Protection Agency (EPA) STAR Grant R835882 awarded to Georgia Institute of Technology. It has not been formally reviewed by the EPA. The views expressed in this document are solely those of the authors and do not necessarily reflect those of the EPA. EPA does not endorse any products or commercial services mentioned in this publication.

7. Competing financial interests

The authors declare no competing financial interests.

8. Data availability

Data can be accessed by request (rweber@eas.gatech.edu).

9. References

Barbier-Jr, J., and Duprez, D.: Steam Effects in 3-way catalysis, *Applied Catalysis B-Environmental*, 4, 105-140, 10.1016/0926-3373(94)80046-4, 1994.

Bertram, A. K., Martin, S. T., Hanna, S. J., Smith, M. L., Bodsworth, A., Chen, Q., Kuwata, M., Liu, A., You, Y., and Zorn, S. R.: Predicting the relative humidities of liquid-liquid phase separation, efflorescence, and deliquescence of mixed particles of ammonium sulfate, organic material, and water using the organic-to-sulfate mass ratio of the particle and the oxygen-to-carbon elemental ratio of the organic component, *Atmos. Chem. Phys.*, 11, 10995-11006, 10.5194/acp-11-10995-2011, 2011.

Blanchard, C. L., Hidy, G. M., Tanenbaum, S., and Edgerton, E. S.: NMOC, ozone, and organic aerosol in the southeastern United States, 1999-2007: 3. Origins of organic aerosol in Atlanta, Georgia, and surrounding areas, *Atmospheric Environment*, 45, 1291-1302, 10.1016/j.atmosenv.2010.12.004, 2011.

Blanchard, C. L., Hidy, G. M., Tanenbaum, S., Edgerton, E. S., and Hartsell, B. E.: The Southeastern Aerosol Research and Characterization (SEARCH) study: Spatial variations and chemical climatology, 1999-2010, *Journal of the Air & Waste Management Association*, 63, 260-275, 10.1080/10962247.2012.749816, 2013a.

Blanchard, C. L., Hidy, G. M., Tanenbaum, S., Edgerton, E. S., and Hartsell, B. E.: The Southeastern Aerosol Research and Characterization (SEARCH) study: Temporal trends in gas and PM concentrations and composition, 1999-2010, *Journal of the Air & Waste Management Association*, 63, 247-259, 10.1080/10962247.2012.748523, 2013b.

781 Blanchard, C. L., Tanenbaum, S., and Hidy, G. M.: Source Attribution of Air Pollutant
 782 Concentrations and Trends in the Southeastern Aerosol Research and Characterization (SEARCH)
 783 Network, *Environmental Science & Technology*, 47, 13536-13545, 10.1021/es402876s, 2013c.

784 Bougiatioti, A., Nikolaou, P., Stavroulas, I., Kouvarakis, G., Weber, R., Nenes, A., Kanakidou,
 785 M., and Mihalopoulos, N.: Particle water and pH in the eastern Mediterranean: source variability
 786 and implications for nutrient availability, *Atmos. Chem. Phys.*, 16, 4579-4591, 10.5194/acp-16-
 787 4579-2016, 2016.

788 Boyd, C. M., Sanchez, J., Xu, L., Eugene, A. J., Nah, T., Tuet, W. Y., Guzman, M. I., and Ng, N.
 789 L.: Secondary organic aerosol formation from the beta-pinene+NO₃ system: effect of humidity
 790 and peroxy radical fate, *Atmos. Chem. Phys.*, 15, 7497-7522, 10.5194/acp-15-7497-2015, 2015.

791 Boyd, C. M., Nah, T., Xu, L., Berkemeier, T., and Ng, N. L.: Secondary Organic Aerosol (SOA)
 792 from Nitrate Radical Oxidation of Monoterpenes: Effects of Temperature, Dilution, and Humidity
 793 on Aerosol Formation, Mixing, and Evaporation, *Environmental Science & Technology*, 51, 7831-
 794 7841, 10.1021/acs.est.7b01460, 2017.

795 Canagaratna, M. R., Jayne, J. T., Jimenez, J. L., Allan, J. D., Alfarra, M. R., Zhang, Q., Onasch,
 796 T. B., Drewnick, F., Coe, H., Middlebrook, A., Delia, A., Williams, L. R., Trimborn, A. M.,
 797 Northway, M. J., DeCarlo, P. F., Kolb, C. E., Davidovits, P., and Worsnop, D. R.: Chemical and
 798 microphysical characterization of ambient aerosols with the aerodyne aerosol mass spectrometer,
 799 *Mass Spectrometry Reviews*, 26, 185-222, 10.1002/mas.20115, 2007.

800 Canagaratna, M. R., Jimenez, J. L., Kroll, J. H., Chen, Q., Kessler, S. H., Massoli, P., Hildebrandt
 801 Ruiz, L., Fortner, E., Williams, L. R., Wilson, K. R., Surratt, J. D., Donahue, N. M., Jayne, J. T.,
 802 and Worsnop, D. R.: Elemental ratio measurements of organic compounds using aerosol mass
 803 spectrometry: characterization, improved calibration, and implications, *Atmos. Chem. Phys.*, 15,
 804 253-272, 10.5194/acp-15-253-2015, 2015.

805 Case, J. L., and Zavodsky, B. T.: Evolution of 2016 drought in the Southeastern United States from
 806 a Land surface modeling perspective, *Results in Physics*, 8, 654-656, 10.1016/j.rinp.2017.12.029,
 807 2018.

808 Chen, J. H., Brooks, C. L., and Scheraga, H. A.: Revisiting the carboxylic acid dimers in aqueous
809 solution: Interplay of hydrogen bonding, hydrophobic interactions, and entropy, *Journal of*
810 *Physical Chemistry B*, 112, 242-249, 10.1021/jp074355h, 2008.

811 Clegg, S. L., and Brimblecombe, P.: Equilibrium partial pressures and mean activity and osmotic
812 coefficients of 0-100-percent nitric- acid as a function of temperature, *Journal of Physical*
813 *Chemistry*, 94, 5369-5380, 10.1021/j100376a038, 1990.

814 Clegg, S. L., Brimblecombe, P., and Khan, L.: The Henry's law constant of oxalic acid and its
815 partitioning into the atmospheric aerosol, *Idojaras*, 100, 51-68, 1996.

816 Clegg, S. L., Brimblecombe, P., and Wexler, A. S.: Thermodynamic model of the system H^+ -
817 NH_4^+ - SO_4^{2-} - NO_3^- - H_2O at tropospheric temperatures, *Journal of Physical Chemistry A*, 102,
818 2137-2154, 10.1021/jp973042r, 1998.

819 DeCarlo, P. F., Kimmel, J. R., Trimborn, A., Northway, M. J., Jayne, J. T., Aiken, A. C., Gonin,
820 M., Fuhrer, K., Horvath, T., Docherty, K. S., Worsnop, D. R., and Jimenez, J. L.: Field-deployable,
821 high-resolution, time-of-flight aerosol mass spectrometer, *Analytical Chemistry*, 78, 8281-8289,
822 10.1021/ac061249n, 2006.

823 Dentener, F. J., and Crutzen, P. J.: A 3-DIMENSIONAL MODEL OF THE GLOBAL AMMONIA
824 CYCLE, *Journal of Atmospheric Chemistry*, 19, 331-369, 10.1007/bf00694492, 1994.

825 Eatough, D. J., Wadsworth, A., Eatough, D. A., Crawford, J. W., Hansen, L. D., and Lewis, E. A.:
826 A multiple-system, multi-channel diffusion denuder sampler for the determination of fine-
827 particulate organic material in the atmosphere, *Atmospheric Environment. Part A. General Topics*,
828 27, 1213-1219, 10.1016/0960-1686(93)90247-V, 1993.

829 Edgerton, E. S., Hartsell, B. E., Saylor, R. D., Jansen, J. J., Hansen, D. A., and Hidy, G. M.: The
830 southeastern aerosol research and characterization study: Part II. Filter-based measurements of
831 fine and coarse particulate matter mass and composition, *Journal of the Air & Waste Management*
832 *Association*, 55, 1527-1542, 2005.

833 Edgerton, E. S., Hartsell, B. E., Saylor, R. D., Jansen, J. J., Hansen, D. A., and Hidy, G. M.: The
834 Southeastern Aerosol Research and Characterization Study, part 3: Continuous measurements of

835 fine particulate matter mass and composition, *Journal of the Air & Waste Management*
836 *Association*, 56, 1325-1341, 10.1080/10473289.2006.10464585, 2006.

837 Edgerton, E. S., Saylor, R. D., Hartsell, B. E., Jansen, J. J., and Hansen, D. A.: Ammonia and
838 ammonium measurements from the southeastern United States, *Atmospheric Environment*, 41,
839 3339-3351, 10.1016/j.atmosenv.2006.12.034, 2007.

840 Ellis, R. A., Murphy, J. G., Markovic, M. Z., VandenBoer, T. C., Makar, P. A., Brook, J., and
841 Mihele, C.: The influence of gas-particle partitioning and surface-atmosphere exchange on
842 ammonia during BAQS-Met, *Atmos. Chem. Phys.*, 11, 133-145, 10.5194/acp-11-133-2011, 2011.

843 Ellis, R. A., Jacob, D. J., Sulprizio, M. P., Zhang, L., Holmes, C. D., Schichtel, B. A., Blett, T.,
844 Porter, E., Pardo, L. H., and Lynch, J. A.: Present and future nitrogen deposition to national parks
845 in the United States: critical load exceedances, *Atmos. Chem. Phys.*, 13, 9083-9095, 10.5194/acp-
846 13-9083-2013, 2013.

847 Ervens, B., Feingold, G., Frost, G. J., and Kreidenweis, S. M.: A modeling study of aqueous
848 production of dicarboxylic acids: 1. Chemical pathways and speciated organic mass production,
849 *Journal of Geophysical Research-Atmospheres*, 109, 10.1029/2003jd004387, 2004.

850 Fountoukis, C., and Nenes, A.: ISORROPIA II: a computationally efficient thermodynamic
851 equilibrium model for $K^+-Ca^{2+}-Mg^{2+}-NH_4^+-Na^+-SO_4^{2-}-NO_3^- -Cl^- -H_2O$ aerosols, *Atmos.*
852 *Chem. Phys.*, 7, 4639-4659, 2007.

853 Gilson, M. K., Given, J. A., Bush, B. L., and McCammon, J. A.: The statistical-thermodynamic
854 basis for computation of binding affinities: A critical review, *Biophysical Journal*, 72, 1047-1069,
855 10.1016/s0006-3495(97)78756-3, 1997.

856 Guenther, A. B., Jiang, X., Heald, C. L., Sakulyanontvittaya, T., Duhl, T., Emmons, L. K., and
857 Wang, X.: The Model of Emissions of Gases and Aerosols from Nature version 2.1 (MEGAN2.1):
858 an extended and updated framework for modeling biogenic emissions, *Geoscientific Model*
859 *Development*, 5, 1471-1492, 10.5194/gmd-5-1471-2012, 2012.

860 Guo, H., Xu, L., Bougiatioti, A., Cerully, K. M., Capps, S. L., Hite, J. R., Jr., Carlton, A. G., Lee,
861 S. H., Bergin, M. H., Ng, N. L., Nenes, A., and Weber, R. J.: Fine-particle water and pH in the

862 southeastern United States, *Atmos. Chem. Phys.*, 15, 5211-5228, 10.5194/acp-15-5211-2015,
863 2015.

864 Guo, H., Sullivan, A. P., Campuzano-Jost, P., Schroder, J. C., Lopez-Hilfiker, F. D., Dibb, J. E.,
865 Jimenez, J. L., Thornton, J. A., Brown, S. S., Nenes, A., and Weber, R. J.: Fine particle pH and
866 the partitioning of nitric acid during winter in the northeastern United States, *Journal of*
867 *Geophysical Research-Atmospheres*, 121, 10355-10376, 10.1002/2016jd025311, 2016.

868 Guo, H., Liu, J. M., Froyd, K. D., Roberts, J. M., Veres, P. R., Hayes, P. L., Jimenez, J. L., Nenes,
869 A., and Weber, R. J.: Fine particle pH and gas-particle phase partitioning of inorganic species in
870 Pasadena, California, during the 2010 CalNex campaign, *Atmos. Chem. Phys.*, 17, 5703-5719,
871 10.5194/acp-17-5703-2017, 2017a.

872 Guo, H., Nenes, A., and Weber, R. J.: The underappreciated role of nonvolatile cations on aerosol
873 ammonium-sulfate molar ratios, *Atmos. Chem. Phys. Discuss.*, 2017, 1-19, 10.5194/acp-2017-
874 737, 2017b.

875 Guo, H., Weber, R. J., and Nenes, A.: High levels of ammonia do not raise fine particle pH
876 sufficiently to yield nitrogen oxide-dominated sulfate production, *Scientific Reports*, 7,
877 10.1038/s41598-017-11704-0, 2017c.

878 Hansen, D. A., Edgerton, E. S., Hartsell, B. E., Jansen, J. J., Kandasamy, N., Hidy, G. M., and
879 Blanchard, C. L.: The southeastern aerosol research and characterization study: Part 1-overview,
880 *Journal of the Air & Waste Management Association*, 53, 1460-1471, 2003.

881 Haynes, W. M.: *CRC handbook of chemistry and physics: A ready-reference book of chemical*
882 *and physical data.* , Boca Raton: CRC Press, 2014.

883 Hennigan, C. J., Izumi, J., Sullivan, A. P., Weber, R. J., and Nenes, A.: A critical evaluation of
884 proxy methods used to estimate the acidity of atmospheric particles, *Atmos. Chem. Phys.*, 15,
885 2775-2790, 10.5194/acp-15-2775-2015, 2015.

886 Huey, L. G., Hanson, D. R., and Howard, C. J.: Reactions of SF₆- and I- with Atmospheric Trace
887 Gases, *Journal of Physical Chemistry*, 99, 5001-5008, 10.1021/j100014a021, 1995.

888 Huey, L. G., Tanner, D. J., Slusher, D. L., Dibb, J. E., Arimoto, R., Chen, G., Davis, D., Buhr, M.
 889 P., Nowak, J. B., Mauldin, R. L., Eisele, F. L., and Kosciuch, E.: CIMS measurements of HNO₃
 890 and SO₂ at the South Pole during ISCAT 2000, *Atmospheric Environment*, 38, 5411-5421,
 891 10.1016/j.atmosenv.2004.04.037, 2004.

892 Kawamura, K., and Gagosian, R. B.: Implication of omega-oxocarboxylic acids in the remote
 893 marine atmosphere for photo-oxidation of unsaturated fatty acids, *Nature*, 325, 330-332,
 894 10.1038/325330a0, 1987.

895 Kawamura, K., and Ikushima, K.: Seasonal changes in the distribution of dicarboxylic acids in the
 896 urban atmosphere, *Environmental Science & Technology*, 27, 2227-2235, 10.1021/es00047a033,
 897 1993.

898 Kawamura, K., and Bikkina, S.: A review of dicarboxylic acids and related compounds in
 899 atmospheric aerosols: Molecular distributions, sources and transformation, *Atmospheric Research*,
 900 170, 140-160, 10.1016/j.atmosres.2015.11.018, 2016.

901 Kerminen, V. M., Ojanen, C., Pakkanen, T., Hillamo, R., Aurela, M., and Merilainen, J.: Low-
 902 molecular-weight dicarboxylic acids in an urban and rural atmosphere, *Journal of Aerosol Science*,
 903 31, 349-362, 10.1016/s0021-8502(99)00063-4, 2000.

904 Lamarque, J. F., Bond, T. C., Eyring, V., Granier, C., Heil, A., Klimont, Z., Lee, D., Lioussé, C.,
 905 Mieville, A., Owen, B., Schultz, M. G., Shindell, D., Smith, S. J., Stehfest, E., Van Aardenne, J.,
 906 Cooper, O. R., Kainuma, M., Mahowald, N., McConnell, J. R., Naik, V., Riahi, K., and van
 907 Vuuren, D. P.: Historical (1850-2000) gridded anthropogenic and biomass burning emissions of
 908 reactive gases and aerosols: methodology and application, *Atmos. Chem. Phys.*, 10, 7017-7039,
 909 10.5194/acp-10-7017-2010, 2010.

910 Laskin, A., Laskin, J., and Nizkorodov, S. A.: Chemistry of Atmospheric Brown Carbon, *Chemical*
 911 *Reviews*, 115, 4335-4382, 10.1021/cr5006167, 2015.

912 Laskin, J., Laskin, A., Roach, P. J., Slys, G. W., Anderson, G. A., Nizkorodov, S. A., Bones, D.
 913 L., and Nguyen, L. Q.: High-Resolution Desorption Electrospray Ionization Mass Spectrometry

914 for Chemical Characterization of Organic Aerosols, *Analytical Chemistry*, 82, 2048-2058,
 915 10.1021/ac902801f, 2010.

916 Lee, B. H., Mohr, C., Lopez-Hilfiker, F. D., Lutz, A., Hallquist, M., Lee, L., Romer, P., Cohen, R.
 917 C., Iyer, S., Kurten, T., Hu, W. W., Day, D. A., Campuzano-Jost, P., Jimenez, J. L., Xu, L., Ng,
 918 N. L., Guo, H. Y., Weber, R. J., Wild, R. J., Brown, S. S., Koss, A., de Gouw, J., Olson, K.,
 919 Goldstein, A. H., Seco, R., Kim, S., McAvey, K., Shepson, P. B., Starn, T., Baumann, K.,
 920 Edgerton, E. S., Liu, J. M., Shilling, J. E., Miller, D. O., Brune, W., Schobesberger, S., D'Ambro,
 921 E. L., and Thornton, J. A.: Highly functionalized organic nitrates in the southeast United States:
 922 Contribution to secondary organic aerosol and reactive nitrogen budgets, *Proceedings of the*
 923 *National Academy of Sciences of the United States of America*, 113, 1516-1521,
 924 10.1073/pnas.1508108113, 2016.

925 Lee, B. P., Li, Y. J., Yu, J. Z., Louie, P. K. K., and Chan, C. K.: Characteristics of submicron
 926 particulate matter at the urban roadside in downtown Hong Kong-Overview of 4 months of
 927 continuous high-resolution aerosol mass spectrometer measurements, *Journal of Geophysical*
 928 *Research-Atmospheres*, 120, 7040-7058, 10.1002/2015jd023311, 2015.

929 Lee, H. J., Laskin, A., Laskin, J., and Nizkorodov, S. A.: Excitation-Emission Spectra and
 930 Fluorescence Quantum Yields for Fresh and Aged Biogenic Secondary Organic Aerosols,
 931 *Environmental Science & Technology*, 47, 5763-5770, 10.1021/es400644c, 2013.

932 Lim, H. J., Carlton, A. G., and Turpin, B. J.: Isoprene forms secondary organic aerosol through
 933 cloud processing: Model simulations, *Environmental Science & Technology*, 39, 4441-4446,
 934 10.1021/es048039h, 2005.

935 Liu, J., Zhang, X., Parker, E. T., Veres, P. R., Roberts, J. M., de Gouw, J. A., Hayes, P. L., Jimenez,
 936 J. L., Murphy, J. G., Ellis, R. A., Huey, L. G., and Weber, R. J.: On the gas-particle partitioning of
 937 soluble organic aerosol in two urban atmospheres with contrasting emissions: 2. Gas and particle
 938 phase formic acid, *Journal of Geophysical Research-Atmospheres*, 117, 10.1029/2012jd017912,
 939 2012.

940 Livingston, C., Rieger, P., and Winer, A.: Ammonia emissions from a representative in-use fleet
 941 of light and medium-duty vehicles in the California South Coast Air Basin, *Atmospheric*
 942 *Environment*, 43, 3326-3333, 10.1016/j.atmosenv.2009.04.009, 2009.

943 Malm, W. C., and Day, D. E.: Estimates of aerosol species scattering characteristics as a function
 944 of relative humidity, *Atmospheric Environment*, 35, 2845-2860, 10.1016/s1352-2310(01)00077-
 945 2, 2001.

946 Middlebrook, A. M., Bahreini, R., Jimenez, J. L., and Canagaratna, M. R.: Evaluation of
 947 Composition-Dependent Collection Efficiencies for the Aerodyne Aerosol Mass Spectrometer
 948 using Field Data, *Aerosol Science and Technology*, 46, 258-271, 10.1080/02786826.2011.620041,
 949 2012.

950 Na, K., Song, C., Switzer, C., and Cocker, D. R.: Effect of ammonia on secondary organic aerosol
 951 formation from alpha-Pinene ozonolysis in dry and humid conditions, *Environmental Science &*
 952 *Technology*, 41, 6096-6102, 10.1021/es061956y, 2007.

953 Nah, T., Ji, Y., Tanner, D. J., Guo, H., Sullivan, A. P., Ng, N. L., Weber, R. J., and Huey, L. G.:
 954 Real-time measurements of gas-phase organic acids using SF₆- chemical ionization mass
 955 spectrometry, *Atmos. Meas. Tech. Discuss.*, 2018, 1-40, 10.5194/amt-2018-46, 2018.

956 Nenes, A., Pandis, S. N., and Pilinis, C.: ISORROPIA: A new thermodynamic equilibrium model
 957 for multiphase multicomponent inorganic aerosols, *Aquatic Geochemistry*, 4, 123-152,
 958 10.1023/a:1009604003981, 1998.

959 Neuman, J. A., Ryerson, T. B., Huey, L. G., Jakoubek, R., Nowak, J. B., Simons, C., and
 960 Fehsenfeld, F. C.: Calibration and evaluation of nitric acid and ammonia permeation tubes by UV
 961 optical absorption, *Environmental Science & Technology*, 37, 2975-2981, 10.1021/es0264221,
 962 2003.

963 Ng, N. L., Brown, S. S., Archibald, A. T., Atlas, E., Cohen, R. C., Crowley, J. N., Day, D. A.,
 964 Donahue, N. M., Fry, J. L., Fuchs, H., Griffin, R. J., Guzman, M. I., Herrmann, H., Hodzic, A.,
 965 Iinuma, Y., Jimenez, J. L., Kiendler-Scharr, A., Lee, B. H., Luecken, D. J., Mao, J. Q., McLaren,
 966 R., Mutzel, A., Osthoff, H. D., Ouyang, B., Picquet-Varraut, B., Platt, U., Pye, H. O. T., Rudich,

967 Y., Schwantes, R. H., Shiraiwa, M., Stutz, J., Thornton, J. A., Tilgner, A., Williams, B. J., and
 968 Zaveri, R. A.: Nitrate radicals and biogenic volatile organic compounds: oxidation, mechanisms,
 969 and organic aerosol, *Atmos. Chem. Phys.*, 17, 2103-2162, 10.5194/acp-17-2103-2017, 2017.

970 Nowak, J. B., Huey, L. G., Eisele, F. L., Tanner, D. J., Mauldin, R. L., Cantrell, C., Kosciuch, E.,
 971 and Davis, D. D.: Chemical ionization mass spectrometry technique for detection of
 972 dimethylsulfoxide and ammonia, *Journal of Geophysical Research-Atmospheres*, 107,
 973 10.1029/2001jd001058, 2002.

974 Nowak, J. B., Huey, L. G., Russell, A. G., Tian, D., Neuman, J. A., Orsini, D., Sjostedt, S. J.,
 975 Sullivan, A. P., Tanner, D. J., Weber, R. J., Nenes, A., Edgerton, E., and Fehsenfeld, F. C.:
 976 Analysis of urban gas phase ammonia measurements from the 2002 Atlanta Aerosol Nucleation
 977 and Real-Time Characterization Experiment (ANARChE), *Journal of Geophysical Research-*
 978 *Atmospheres*, 111, 14, 10.1029/2006jd007113, 2006.

979 Orsini, D. A., Ma, Y. L., Sullivan, A., Sierau, B., Baumann, K., and Weber, R. J.: Refinements to
 980 the particle-into-liquid sampler (PILS) for ground and airborne measurements of water soluble
 981 aerosol composition, *Atmospheric Environment*, 37, 1243-1259, 10.1016/s1352-2310(02)01015-
 982 4, 2003.

983 Park Williams, A., Cook, B. I., Smerdon, J. E., Bishop, D. A., Seager, R., and Mankin, J. S.: The
 984 2016 Southeastern U.S. Drought: An Extreme Departure From Centennial Wetting and Cooling,
 985 *Journal of Geophysical Research: Atmospheres*, 122, 10,888-810,905, 10.1002/2017JD027523,
 986 2017.

987 Pechony, O., and Shindell, D. T.: Driving forces of global wildfires over the past millennium and
 988 the forthcoming century, *Proceedings of the National Academy of Sciences of the United States*
 989 *of America*, 107, 19167-19170, 10.1073/pnas.1003669107, 2010.

990 Pye, H. O. T., Luecken, D. J., Xu, L., Boyd, C. M., Ng, N. L., Baker, K. R., Ayres, B. R., Bash, J.
 991 O., Baumann, K., Carter, W. P. L., Edgerton, E., Fry, J. L., Hutzell, W. T., Schwede, D. B., and
 992 Shepson, P. B.: Modeling the Current and Future Roles of Particulate Organic Nitrates in the
 993 Southeastern United States, *Environmental Science & Technology*, 49, 14195-14203,
 994 10.1021/acs.est.5b03738, 2015.

995 Reis, S., Pinder, R. W., Zhang, M., Lijie, G., and Sutton, M. A.: Reactive nitrogen in atmospheric
 996 emission inventories, *Atmos. Chem. Phys.*, 9, 7657-7677, 10.5194/acp-9-7657-2009, 2009.

997 Sander, R.: Compilation of Henry's law constants (version 4.0) for water as solvent, *Atmos. Chem.*
 998 *Phys.*, 15, 4399-4981, 10.5194/acp-15-4399-2015, 2015.

999 Saxena, P., and Hildemann, L. M.: Water-soluble organics in atmospheric particles: A critical
 1000 review of the literature and application of thermodynamics to identify candidate compounds,
 1001 *Journal of Atmospheric Chemistry*, 24, 57-109, 10.1007/bf00053823, 1996.

1002 Saylor, R., Myles, L., Sibble, D., Caldwell, J., and Xing, J.: Recent trends in gas-phase ammonia
 1003 and PM_{2.5} ammonium in the Southeast United States, *Journal of the Air & Waste Management*
 1004 *Association*, 65, 347-357, 10.1080/10962247.2014.992554, 2015.

1005 Schrier, E. E., Pottle, M., and Scheraga, H. A.: The Influence of Hydrogen and Hydrophobic Bonds
 1006 on the Stability of the Carboxylic Acid Dimers in Aqueous Solution, *Journal of the American*
 1007 *Chemical Society*, 86, 3444-3449, 10.1021/ja01071a009, 1964.

1008 Seinfeld, J. H., and Pandis, S. N.: *Atmospheric chemistry and physics : from air pollution to*
 1009 *climate change*, Third edition. ed., John Wiley & Sons, Inc., Hoboken, New Jersey, xxvi, 1120
 1010 pages pp., 2016.

1011 Shi, G. L., Xu, J., Peng, X., Xiao, Z. M., Chen, K., Tian, Y. Z., Guan, X. B., Feng, Y. C., Yu, H.
 1012 F., Nenes, A., and Russell, A. G.: pH of Aerosols in a Polluted Atmosphere: Source Contributions
 1013 to Highly Acidic Aerosol, *Environmental Science & Technology*, 51, 4289-4296,
 1014 10.1021/acs.est.6b05736, 2017.

1015 Song, M., Marcolli, C., Krieger, U. K., Zuend, A., and Peter, T.: Liquid-liquid phase separation
 1016 and morphology of internally mixed dicarboxylic acids/ammonium sulfate/water particles, *Atmos.*
 1017 *Chem. Phys.*, 12, 2691-2712, 10.5194/acp-12-2691-2012, 2012.

1018 Song, S., Gao, M., Xu, W., Shao, J., Shi, G., Wang, S., Wang, Y., Sun, Y., and McElroy, M. B.:
 1019 Fine particle pH for Beijing winter haze as inferred from different thermodynamic equilibrium
 1020 models, *Atmos. Chem. Phys. Discuss.*, 2018, 1-26, 10.5194/acp-2018-6, 2018.

1021 Sorooshian, A., Ng, N. L., Chan, A. W. H., Feingold, G., Flagan, R. C., and Seinfeld, J. H.:
 1022 Particulate organic acids and overall water-soluble aerosol composition measurements from the
 1023 2006 Gulf of Mexico Atmospheric Composition and Climate Study (GoMACCS), *Journal of*
 1024 *Geophysical Research-Atmospheres*, 112, 16, 10.1029/2007jd008537, 2007.

1025 Sorooshian, A., Murphy, S. M., Hersey, S., Bahreini, R., Jonsson, H., Flagan, R. C., and Seinfeld,
 1026 J. H.: Constraining the contribution of organic acids and AMS m/z 44 to the organic aerosol
 1027 budget: On the importance of meteorology, aerosol hygroscopicity, and region, *Geophys. Res.*
 1028 *Lett.*, 37, 5, 10.1029/2010gl044951, 2010.

1029 Spaulding, R. S., Talbot, R. W., and Charles, M. J.: Optimization of a mist chamber (cofer
 1030 scrubber) for sampling water-soluble organics in air, *Environmental Science & Technology*, 36,
 1031 1798-1808, 10.1021/es011189x, 2002.

1032 Suarez-Bertoa, R., Zardini, A. A., and Astorga, C.: Ammonia exhaust emissions from spark
 1033 ignition vehicles over the New European Driving Cycle, *Atmospheric Environment*, 97, 43-53,
 1034 10.1016/j.atmosenv.2014.07.050, 2014.

1035 Sullivan, A. P., Weber, R. J., Clements, A. L., Turner, J. R., Bae, M. S., and Schauer, J. J.: A
 1036 method for on-line measurement of water-soluble organic carbon in ambient aerosol particles:
 1037 Results from an urban site, *Geophysical Research Letters*, 31, 10.1029/2004gl019681, 2004.

1038 Sun, K., Tao, L., Miller, D. J., Pan, D., Golston, L. M., Zondlo, M. A., Griffin, R. J., Wallace, H.
 1039 W., Leong, Y. J., Yang, M. M., Zhang, Y., Mauzerall, D. L., and Zhu, T.: Vehicle Emissions as an
 1040 Important Urban Ammonia Source in the United States and China, *Environmental Science &*
 1041 *Technology*, 51, 2472-2481, 10.1021/acs.est.6b02805, 2017.

1042 Updyke, K. M., Nguyen, T. B., and Nizkorodov, S. A.: Formation of brown carbon via reactions
 1043 of ammonia with secondary organic aerosols from biogenic and anthropogenic precursors,
 1044 *Atmospheric Environment*, 63, 22-31, 10.1016/j.atmosenv.2012.09.012, 2012.

1045 Van Damme, M., Clarisse, L., Heald, C. L., Hurtmans, D., Ngadi, Y., Clerbaux, C., Dolman, A.
 1046 J., Erisman, J. W., and Coheur, P. F.: Global distributions, time series and error characterization

1047 of atmospheric ammonia (NH₃) from IASI satellite observations, *Atmos. Chem. Phys.*, 14, 2905-
 1048 2922, 10.5194/acp-14-2905-2014, 2014.

1049 Warner, J. X., Wei, Z. G., Strow, L. L., Dickerson, R. R., and Nowak, J. B.: The global
 1050 tropospheric ammonia distribution as seen in the 13-year AIRS measurement record, *Atmos.*
 1051 *Chem. Phys.*, 16, 5467-5479, 10.5194/acp-16-5467-2016, 2016.

1052 Warner, J. X., Dickerson, R. R., Wei, Z., Strow, L. L., Wang, Y., and Liang, Q.: Increased
 1053 atmospheric ammonia over the world's major agricultural areas detected from space, *Geophysical*
 1054 *Research Letters*, 44, 2875-2884, 10.1002/2016gl072305, 2017.

1055 Weber, R. J., Orsini, D., Daun, Y., Lee, Y. N., Klotz, P. J., and Brechtel, F.: A particle-into-liquid
 1056 collector for rapid measurement of aerosol bulk chemical composition, *Aerosol Science and*
 1057 *Technology*, 35, 718-727, 10.1080/02786820152546761, 2001.

1058 Weber, R. J., Lee, S., Chen, G., Wang, B., Kapustin, V., Moore, K., Clarke, A. D., Mauldin, L.,
 1059 Kosciuch, E., Cantrell, C., Eisele, F., Thornton, D. C., Bandy, A. R., Sachse, G. W., and Fuelberg,
 1060 H. E.: New particle formation in anthropogenic plumes advecting from Asia observed during
 1061 TRACE-P, *Journal of Geophysical Research-Atmospheres*, 108, 13, 10.1029/2002jd003112,
 1062 2003.

1063 Weber, R. J., Guo, H., Russell, A. G., and Nenes, A.: High aerosol acidity despite declining
 1064 atmospheric sulfate concentrations over the past 15 years, *Nature Geoscience*, 9, 282-+,
 1065 10.1038/ngeo2665, 2016.

1066 Whittington, B. I., Jiang, C. J., and Trimm, D. L.: Vehicle exhaust catalysis: I. The relative
 1067 importance of catalytic oxidation, steam reforming and water-gas shift reactions, *Catalysis Today*,
 1068 26, 41-45, 10.1016/0920-5861(95)00093-u, 1995.

1069 Xing, J., Pleim, J., Mathur, R., Pouliot, G., Hogrefe, C., Gan, C. M., and Wei, C.: Historical
 1070 gaseous and primary aerosol emissions in the United States from 1990 to 2010, *Atmos. Chem.*
 1071 *Phys.*, 13, 7531-7549, 10.5194/acp-13-7531-2013, 2013.

1072 Xu, L., Guo, H., Boyd, C. M., Klein, M., Bougiatioti, A., Cerully, K. M., Hite, J. R., Isaacman-
 1073 VanWertz, G., Kreisberg, N. M., Knote, C., Olson, K., Koss, A., Goldstein, A. H., Hering, S. V.,

1074 de Gouw, J., Baumann, K., Lee, S.-H., Nenes, A., Weber, R. J., and Ng, N. L.: Effects of
 1075 anthropogenic emissions on aerosol formation from isoprene and monoterpenes in the southeastern
 1076 United States, *Proceedings of the National Academy of Sciences of the United States of America*,
 1077 112, 37-42, 10.1073/pnas.1417609112, 2015a.

1078 Xu, L., Suresh, S., Guo, H., Weber, R. J., and Ng, N. L.: Aerosol characterization over the
 1079 southeastern United States using high-resolution aerosol mass spectrometry: spatial and seasonal
 1080 variation of aerosol composition and sources with a focus on organic nitrates, *Atmos. Chem. Phys.*,
 1081 15, 7307-7336, 10.5194/acp-15-7307-2015, 2015b.

1082 Xu, L., Guo, H. Y., Weber, R. J., and Ng, N. L.: Chemical Characterization of Water-Soluble
 1083 Organic Aerosol in Contrasting Rural and Urban Environments in the Southeastern United States,
 1084 *Environmental Science & Technology*, 51, 78-88, 10.1021/acs.est.6b05002, 2017.

1085 Yao, X. H., Hu, Q. J., Zhang, L. M., Evans, G. J., Godri, K. J., and Ng, A. C.: Is vehicular emission
 1086 a significant contributor to ammonia in the urban atmosphere?, *Atmospheric Environment*, 80,
 1087 499-506, 10.1016/j.atmosenv.2013.08.028, 2013.

1088 You, Y., Renbaum-Wolff, L., and Bertram, A. K.: Liquid-liquid phase separation in particles
 1089 containing organics mixed with ammonium sulfate, ammonium bisulfate, ammonium nitrate or
 1090 sodium chloride, *Atmos. Chem. Phys.*, 13, 11723-11734, 10.5194/acp-13-11723-2013, 2013.

1091 You, Y., Kanawade, V. P., de Gouw, J. A., Guenther, A. B., Madronich, S., Sierra-Hernandez, M.
 1092 R., Lawler, M., Smith, J. N., Takahama, S., Ruggeri, G., Koss, A., Olson, K., Baumann, K., Weber,
 1093 R. J., Nenes, A., Guo, H., Edgerton, E. S., Porcelli, L., Brune, W. H., Goldstein, A. H., and Lee,
 1094 S. H.: Atmospheric amines and ammonia measured with a chemical ionization mass spectrometer
 1095 (CIMS), *Atmos. Chem. Phys.*, 14, 12181-12194, 10.5194/acp-14-12181-2014, 2014a.

1096 You, Y., Smith, M. L., Song, M., Martin, S. T., and Bertram, A. K.: Liquid-liquid phase separation
 1097 in atmospherically relevant particles consisting of organic species and inorganic salts, *International*
 1098 *Reviews in Physical Chemistry*, 33, 43-77, 10.1080/0144235x.2014.890786, 2014b.

1099 You, Y., and Bertram, A. K.: Effects of molecular weight and temperature on liquid-liquid phase
 1100 separation in particles containing organic species and inorganic salts, *Atmos. Chem. Phys.*, 15,
 1101 1351-1365, 10.5194/acp-15-1351-2015, 2015.

1102 Yu, H., and Lee, S. H.: Chemical ionisation mass spectrometry for the measurement of
 1103 atmospheric amines, *Environ. Chem.*, 9, 190-201, 10.1071/en12020, 2012.

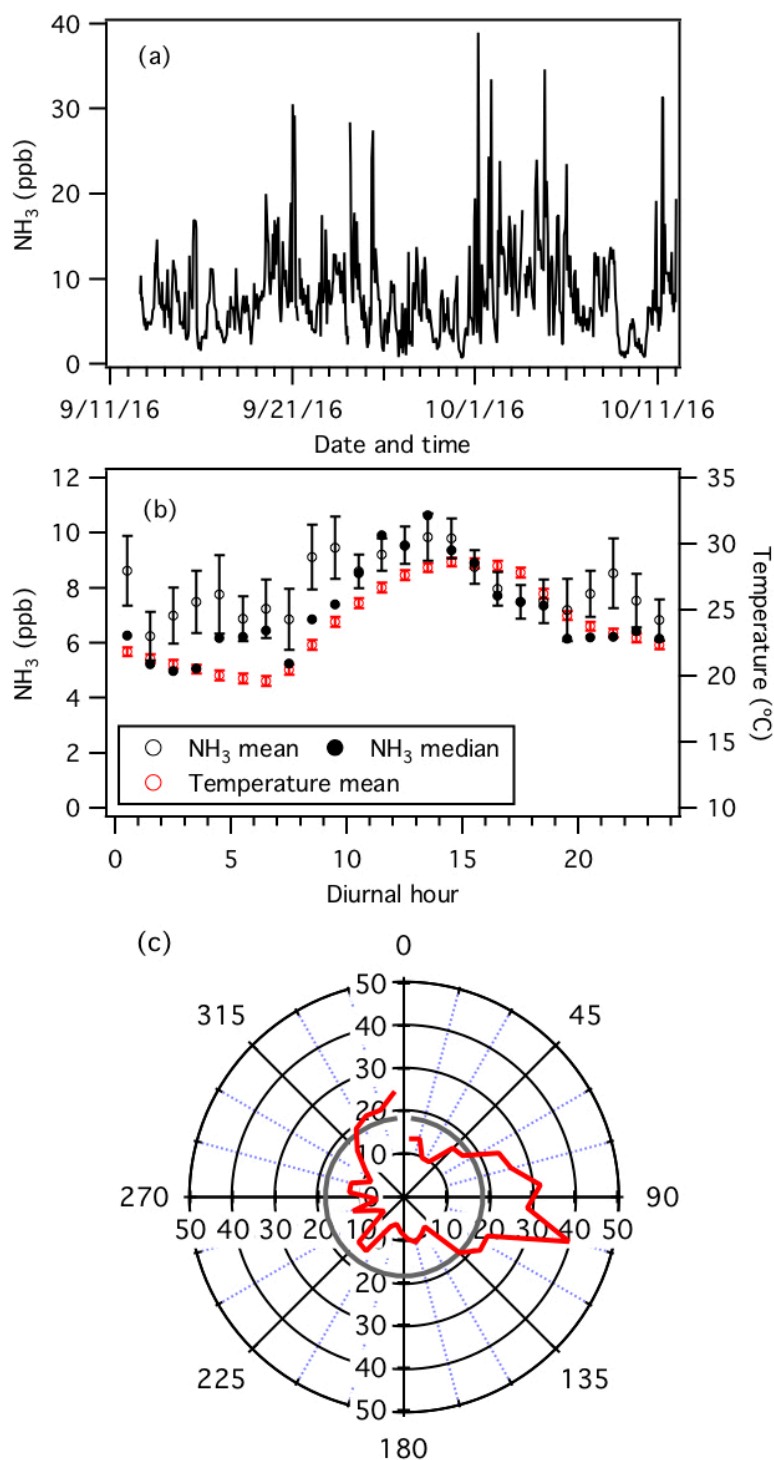
1104 Zhang, H. F., Yee, L. D., Lee, B. H., Curtis, M. P., Worton, D. R., Isaacman-VanWertz, G.,
 1105 Offenberg, J. H., Lewandowski, M., Kleindienst, T. E., Beaver, M. R., Holder, A. L., Lonneman,
 1106 W. A., Docherty, K. S., Jaoui, M., Pye, H. O. T., Hu, W. W., Day, D. A., Campuzano-Jost, P.,
 1107 Jimenez, J. L., Guo, H. Y., Weber, R. J., de Gouw, J., Koss, A. R., Edgerton, E. S., Brune, W.,
 1108 Mohr, C., Lopez-Hilfiker, F. D., Lutz, A., Kreisberg, N. M., Spielman, S. R., Hering, S. V., Wilson,
 1109 K. R., Thornton, J. A., and Goldstein, A. H.: Monoterpenes are the largest source of summertime
 1110 organic aerosol in the southeastern United States, *Proceedings of the National Academy of*
 1111 *Sciences of the United States of America*, 115, 2038-2043, 10.1073/pnas.1717513115, 2018.

1112 Zuend, A., Marcolli, C., Luo, B. P., and Peter, T.: A thermodynamic model of mixed organic-
 1113 inorganic aerosols to predict activity coefficients, *Atmos. Chem. Phys.*, 8, 4559-4593,
 1114 10.5194/acp-8-4559-2008, 2008.

1115 Zuend, A., Marcolli, C., Booth, A. M., Lienhard, D. M., Soonsin, V., Krieger, U. K., Topping, D.
 1116 O., McFiggans, G., Peter, T., and Seinfeld, J. H.: New and extended parameterization of the
 1117 thermodynamic model AIOMFAC: calculation of activity coefficients for organic-inorganic
 1118 mixtures containing carboxyl, hydroxyl, carbonyl, ether, ester, alkenyl, alkyl, and aromatic
 1119 functional groups, *Atmos. Chem. Phys.*, 11, 9155-9206, 10.5194/acp-11-9155-2011, 2011.

1120 Zuend, A., Marcolli, C., Luo, B. P., and Peter, T.: A thermodynamic model of mixed organic-
 1121 inorganic aerosols to predict activity coefficients (vol 8, pg 4559, 2008), *Atmos. Chem. Phys.*, 12,
 1122 10075-10075, 10.5194/acp-12-10075-2012, 2012.

1123



1124

1125 **Figure 1:** Measurements by the NH_3 -CIMS during the second half of the study. (a) Time series of
 1126 NH_3 concentration. The data is displayed as 1-hour averages. (b) Diurnal profiles of NH_3
 1127 concentration (mean and median) and temperature. Error bars shown are the standard errors. Dates
 1128 and times displayed are local time. All the concentrations represent averages in 1-hour intervals

and the standard errors are plotted as error bars. (c) Average NH_3 concentration normalized to wind speed (i.e., NH_3 concentration (ppb) \times wind speed (m s^{-1})) in each 10 degrees bin (red line). The average normalized NH_3 concentration is shown as a grey line.

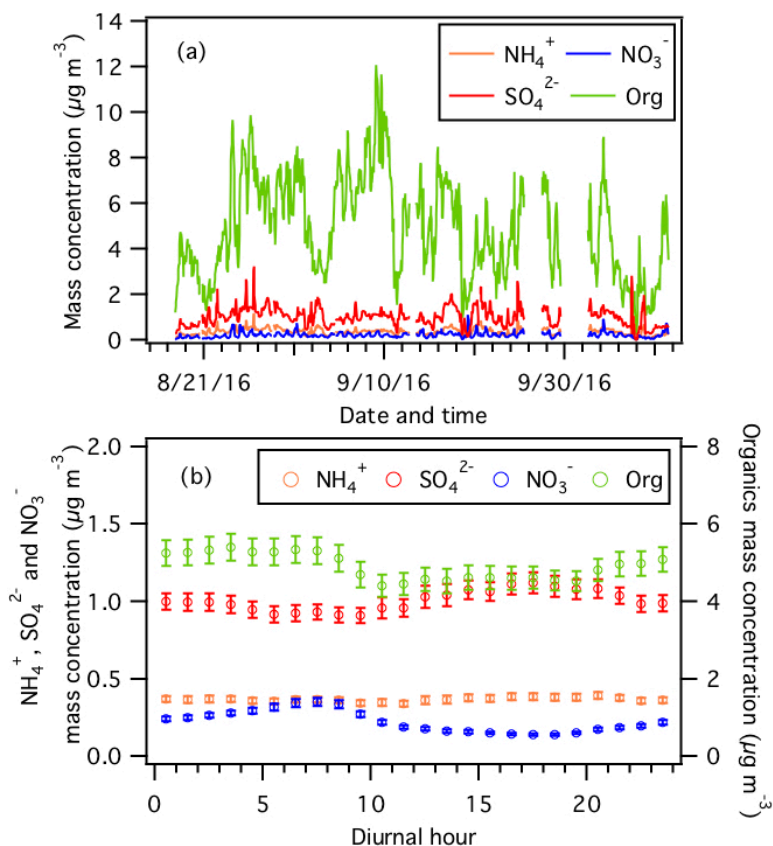
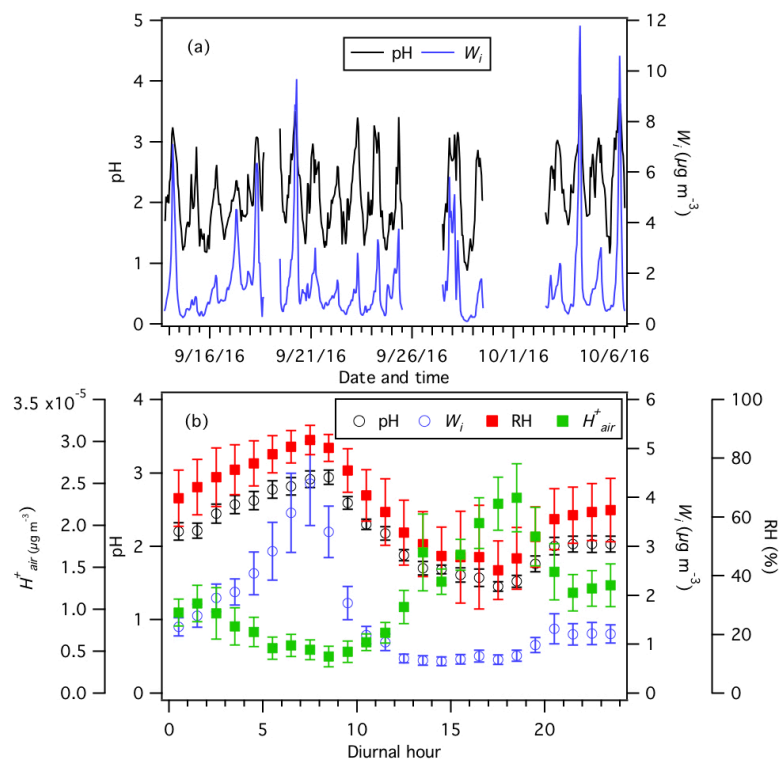
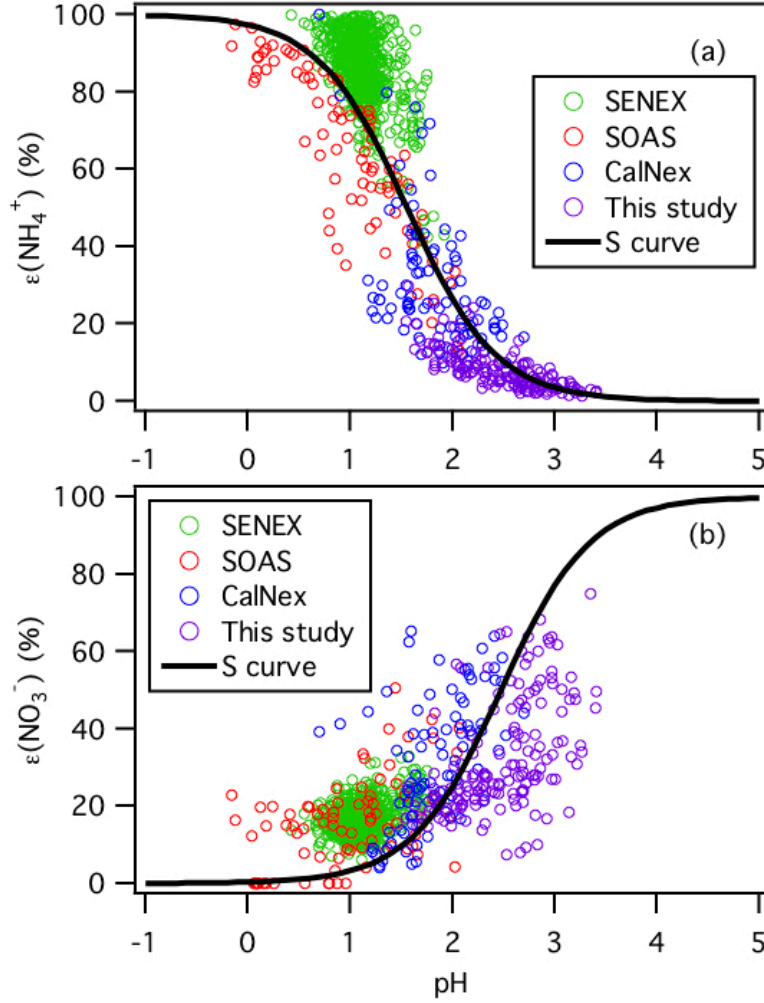


Figure 2: (a) Time series and (b) diurnal profiles of non-refractory PM_{10} species measured by the AMS. Error bars shown in panel (b) are the standard errors. Dates and times displayed are local time.



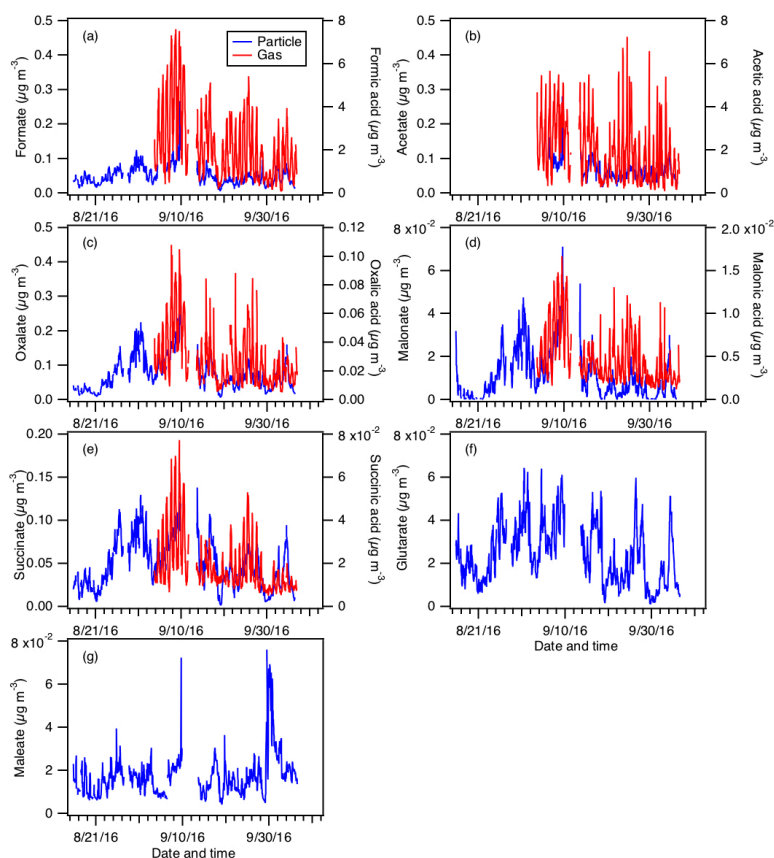
1137

1138 **Figure 3:** (a) Time series and (b) diurnal profiles of ISORROPIA-predicted PM_{10} pH and W_i . The
 1139 diurnal profiles of RH and ISORROPIA-predicted H_{air}^+ are also shown in panel (b). Dates and
 1140 times displayed are local time. All the data shown here represent averages in 1-hour intervals.
 1141 Error bars shown in panel (b) are the standard errors.



1142

1143 **Figure 4:** Analytically calculated S curves of $\epsilon(\text{NH}_4^+)$ and $\epsilon(\text{NO}_3^-)$ and ambient data plotted
 1144 against ISORROPIA-predicted particle pH for this study, SENEX, SOAS and CalNex. For the
 1145 ambient datasets, a narrow range of W_i (1 to 4 $\mu\text{g m}^{-3}$) and temperature (15 to 25 $^\circ\text{C}$) are selected
 1146 to be close to the analytical calculation input (i.e., $W_i = 2.5 \mu\text{g m}^{-3}$ and temperature = 20 $^\circ\text{C}$).
 1147 Similar to Guo et al. (2017a), $\gamma_{\text{NH}_4^+} = 1$ and $\gamma_{\text{H}^+ - \text{NO}_3^-} = \sqrt{\gamma_{\text{H}^+} \gamma_{\text{NO}_3^-}} = 0.28$ are used for the
 1148 analytically calculated S curves.



1149

1150 **Figure 5:** Particle- and gas-phase measurements of (a) formic, (b) acetic, (c) oxalic, (d) malonic,
 1151 (e) succinic, (f) glutaric, and (g) maleic acids. Particle-phase measurements are shown on the left
 1152 y axes, while gas-phase measurements are shown on the right y axes. Dates and times displayed
 1153 are local time. Gas-phase measurements of glutaric and maleic acids are not available.

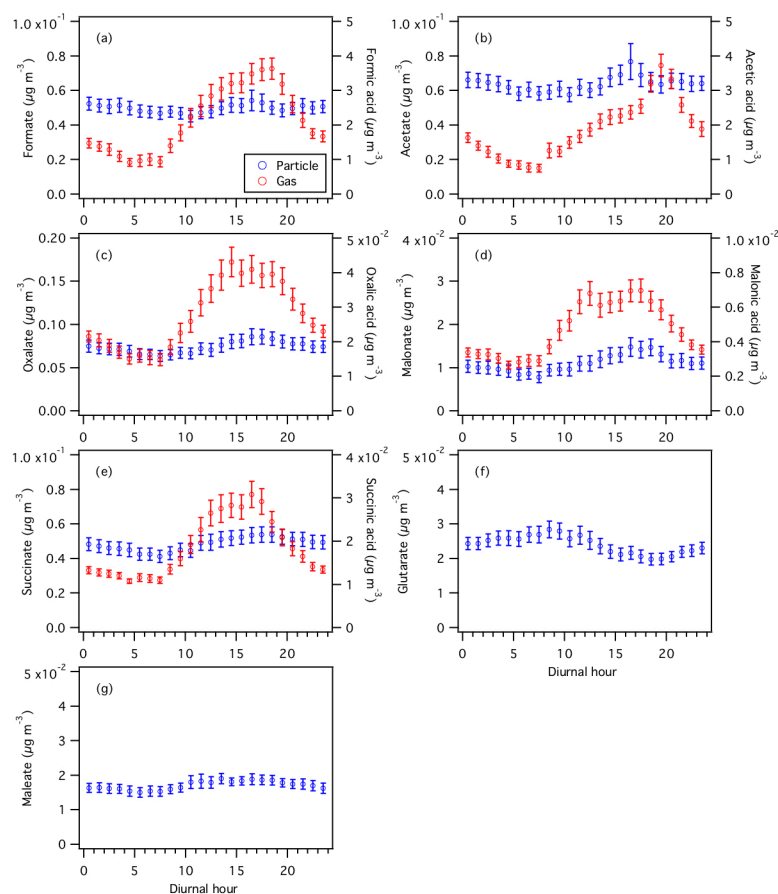


Figure 6: Diurnal profiles of particle- and gas-phase (a) formic, (b) acetic, (c) oxalic, (d) malonic, (e) succinic, (f) glutaric, and (g) maleic acids. Particle-phase measurements are shown on the left y axes, while gas-phase measurements are shown on the right y axes. All the data shown here represent averages in 1-hour intervals. Error bars shown are the standard errors.

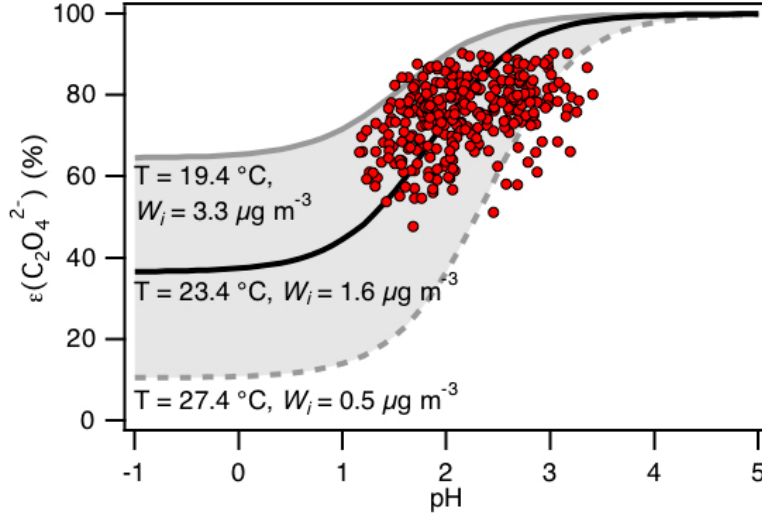
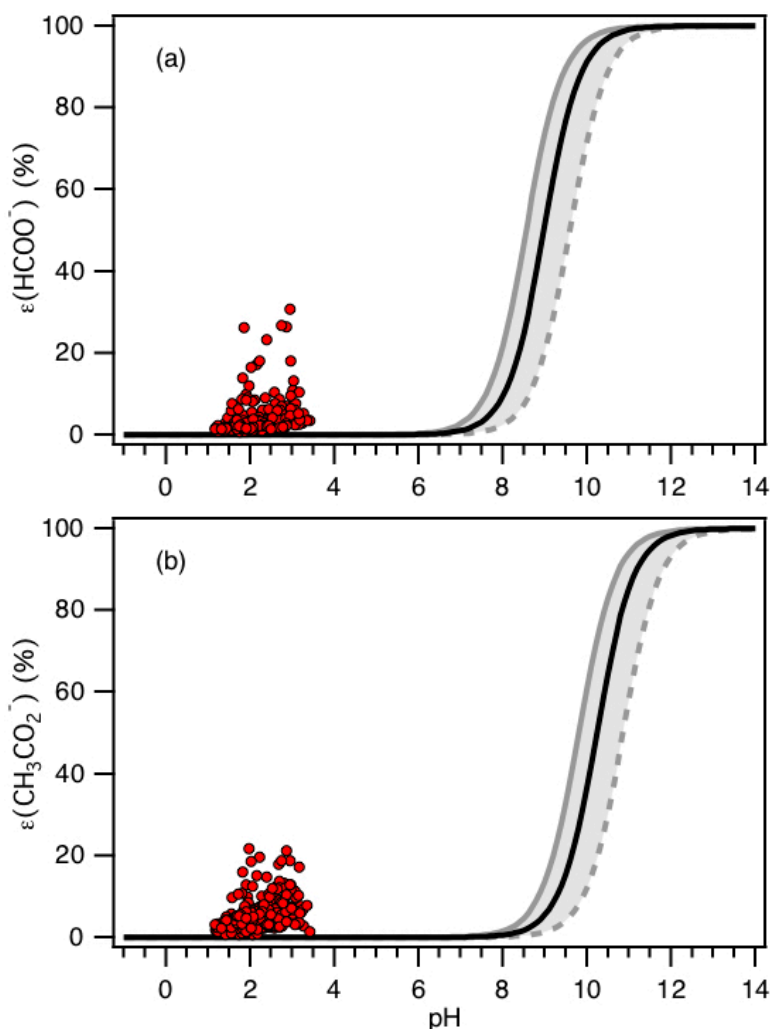


Figure 7: Analytically calculated S curve of $\varepsilon(\text{C}_2\text{O}_4^{2-})$ and ambient data from 13 September to 6 October 2016 plotted against ISORROPIA-predicted particle pH. For the ambient data, a range in W_i (0.5 to $4 \mu\text{g m}^{-3}$) and temperature (15 to $31 \text{ }^\circ\text{C}$) are chosen to be close to the analytically calculated outputs. For the analytically calculated S curves, we used $\gamma_{\text{C}_2\text{H}_2\text{O}_4} = 0.0492$ (AIOMFAC predicted). We also assumed that $\gamma_{\text{H}^+}\gamma_{\text{C}_2\text{HO}_4^-} = \gamma_{\text{H}^+}\gamma_{\text{NO}_3^-}$, and used the ISORROPIA-predicted $\gamma_{\text{H}^+}\gamma_{\text{NO}_3^-} = \sqrt{\gamma_{\text{H}^+}\gamma_{\text{NO}_3^-}} = 0.265$. The black line is the S curve calculated using the selected time period's average temperature ($23.4 \pm 4.0 \text{ }^\circ\text{C}$) and W_i ($1.6 \pm 1.7 \mu\text{g m}^{-3}$). The grey lines are S curves calculated using one standard deviation from the average temperature and W_i (i.e., temperature = $27.4 \text{ }^\circ\text{C}$ and $W_i = 0.5 \mu\text{g m}^{-3}$ for dotted grey line, temperature = $19.4 \text{ }^\circ\text{C}$ and $W_i = 3.3 \mu\text{g m}^{-3}$ for solid grey line).



1172

1173 **Figure 8:** Analytically calculated S curves of $\varepsilon(\text{HCOO}^-)$ and $\varepsilon(\text{CH}_3\text{CO}_2^-)$ (solid black lines) and
 1174 ambient data from 13 September to 6 October 2016 plotted against ISORROPIA-predicted particle
 1175 pH (shown in panels (a) and (b), respectively). For the ambient data, a narrow range in W_i (0.5 to
 1176 $4 \mu\text{g m}^{-3}$) and RH (20 to 90 %) is chosen to be close to the analytically calculated outputs. For the
 1177 analytically calculated S curves, we used $\gamma_{\text{HCOOH}} = 0.334$ and $\gamma_{\text{CH}_3\text{COOH}} = 2.150$ (AIOMFAC
 1178 predicted). We also assumed that $\gamma_{\text{H}^+}\gamma_{\text{HCOO}^-} = \gamma_{\text{H}^+}\gamma_{\text{CH}_3\text{COO}^-} = \gamma_{\text{H}^+}\gamma_{\text{NO}_3^-}$, and used the
 1179 ISORROPIA-predicted $\gamma_{\text{H}^+}\gamma_{\text{NO}_3^-} = \sqrt{\gamma_{\text{H}^+}\gamma_{\text{NO}_3^-}} = 0.265$. The black lines are S curves calculated
 1180 using the selected time period's average temperature ($23.4 \pm 4.0 \text{ }^\circ\text{C}$) and W_i ($1.6 \pm 1.7 \mu\text{g m}^{-3}$).
 1181 The grey lines are S curves calculated using one standard deviation from the average temperature
 1182 and W_i (i.e., temperature = $27.4 \text{ }^\circ\text{C}$ and $W_i = 0.5 \mu\text{g m}^{-3}$ for dotted grey line, temperature = 19.4
 1183 $^\circ\text{C}$ and $W_i = 3.3 \mu\text{g m}^{-3}$ for solid grey line).

Table 1: Comparisons between different field campaigns for particle pH, major inorganic ions and gases and meteorological conditions. All pH values were calculated using ISORROPIA-II run in forward mode. These statistics were previously compiled by Guo et al. (2017a). Campaign acronyms used here stand for the California Research at the Nexus of Air Quality and Climate Change (CalNex), Southern Oxidant and Aerosol Study (SOAS), and Southeastern Nexus of Air Quality and Climate (SENEX).

Campaign	CalNex		SOAS	SENEX	This study
Type	Ground		Ground	Aircraft	Ground
PM cut size	PM ₁	PM _{2.5} ^a	PM ₁ &PM _{2.5} ^b	PM ₁	PM ₁
Year	2010		2013	2013	2016
Season	(Early Summer)		Summer	Summer	Fall
Region/Location	SW US		SE US	SE US	SE US
SO ₄ ²⁻ , µg m ⁻³	2.86 ± 1.70	1.88 ± 0.69	1.73 ± 1.21	2.05 ± 0.80	1.6 ± 0.4
NO ₃ ⁻ , µg m ⁻³	3.58 ± 3.65	3.74 ± 1.53	0.08 ± 0.08	0.28 ± 0.09	0.20 ± 0.10
HNO ₃ , µg m ⁻³	6.65 ± 7.03	4.45 ± 3.59	0.36 ± 0.14	1.35 ± 0.66	0.50 ± 0.26
ε(NO ₃ ⁻)	39 ± 16 %	51 ± 18 %	22 ± 16 %	18 ± 6 %	26 ± 15 %
Total NO ₃ ⁻ , µg m ⁻³	10.22 ± 9.74	8.19 ± 3.89	0.45 ± 0.26	1.63 ± 0.70	0.70 ± 0.28
NH ₄ ⁺ , µg m ⁻³	2.06 ± 1.67	1.79 ± 0.65	0.46 ± 0.34	1.06 ± 0.25	0.40 ± 0.20
NH ₃ , µg m ⁻³	1.37 ± 0.90	0.75 ± 0.61	0.39 ± 0.25	0.12 ± 0.19	5.79 ± 3.67
ε(NH ₄ ⁺)	55 ± 25%	71 ± 19%	50 ± 25%	92 ± 11%	7 ± 5 %
Total NH ₄ ⁺ , µg m ⁻³	3.44 ± 1.81	2.54 ± 0.89	0.78 ± 0.50	1.17 ± 0.81	6.19 ± 3.68
Na ⁺ , µg m ⁻³	\	0.77 ± 0.39	0.03 ± 0.07	\	\
Cl ⁻ , µgm ⁻³	\	0.64 ± 0.48	0.02 ± 0.03	\	0.01 ± 0.01
RH, %	79 ± 17	87 ± 9	74 ± 16	72 ± 9	69 ± 18
T, °C	18 ± 4	18 ± 3	25 ± 3	22 ± 3	24 ± 4
W _i , µg m ⁻³	13.9 ± 18.1	29.8 ± 20.7	5.1 ± 3.8	3.2 ± 2.8	1.6 ± 1.7
pH	1.9 ± 0.5	2.7 ± 0.3	0.9 ± 0.6	1.1 ± 0.4	2.2 ± 0.6
Reference	(Guo et al., 2017a)		(Guo et al., 2015)	(Xu et al., 2016)	This study

^aOnly during the last week of CalNex.

^bPM_{2.5} was sampled in the first half and PM₁ sampled in the second half of the study. Various parameters were similar in both cases. Crustal components were higher, but are overall generally in low concentrations so the differences had minor effects. For example, PM_{2.5} Na⁺ was 0.06 ± 0.09 µg m⁻³ and PM₁ Na⁺ was 0.01 ± 0.01 µg m⁻³.